Malic Enzyme 1 Absence in Synovial Sarcoma Shifts Antioxidant System Dependence and Increases Sensitivity to Ferroptosis Induction with ACXT-3102

Caitlyn B. Brashears[1], Bethany C. Prudner[1], Richa Rathore[1], Katharine E. Caldwell[2], Carina A. Dehner[3], Jane L. Buchanan[4], Sara E.S. Lange[1], Neal Poulin[5], Jennifer K. Sehn[3], Jason Roszik[6], Dirk Spitzer[2,7], Kevin B. Jones[8,9,10], Regis O'Keefe[7,11], Torsten O. Nielsen[5], Eric B. Taylor[4,12,13], Jason M. Held[1,7,14], William Hawkins[2,7], and Brian A. Van Tine[1,7,15]

ABSTRACT

Purpose: To investigate the metabolism of synovial sarcoma (SS) and elucidate the effect of malic enzyme 1 absence on SS redox homeostasis.

Experimental Design: ME1 expression was measured in SS clinical samples, SS cell lines, and tumors from an SS mouse model. The effect of ME1 absence on glucose metabolism was evaluated utilizing Seahorse assays, metabolomics, and C^{13} tracings. The impact of ME1 absence on SS redox homeostasis was evaluated by metabolomics, cell death assays with inhibitors of antioxidant systems, and measurements of intracellular reactive oxygen species (ROS). The susceptibility of ME1-null SS to ferroptosis induction was interrogated *in vitro* and *in vivo*.

Results: ME1 absence in SS was confirmed in clinical samples, SS cell lines, and an SS tumor model. Investigation of SS glucose metabolism revealed that ME1-null cells exhibit higher rates of glycolysis and higher flux of glucose into the pentose phosphate pathway (PPP), which is necessary to produce NADPH. Evaluation of cellular redox homeostasis demonstrated that ME1 absence shifts dependence from the glutathione system to the thioredoxin system. Concomitantly, ME1 absence drives the accumulation of ROS and labile iron. ROS and iron accumulation enhances the susceptibility of ME1-null cells to ferroptosis induction with inhibitors of xCT (erastin and ACXT-3102). *In vivo* xenograft models of ME1-null SS demonstrate significantly increased tumor response to ACXT-3102 compared with ME1-expressing controls.

Conclusions: These findings demonstrate the translational potential of targeting redox homeostasis in ME1-null cancers and establish the preclinical rationale for a phase I trial of ACXT-3102 in SS patients.

See related commentary by Subbiah and Gan, p. 3408

Introduction

Synovial sarcoma (SS) is the most common translocation-driven soft-tissue sarcoma (1). It is characterized by a gene fusion between the transcription factor *SS18* (formerly termed *SYT*) on chromosome 18 and one of three homologous genes (*SSX1*, *SSX2*, or *SSX4*) on the X chromosome (2–4). The t(X;18) translocation has been identified in 90% to 95% of all cases of SS and is pathognomonic for the disease (5). There are approximately 900 to 1,000 cases per year in the United States, accounting for 8% to 10% of all soft-tissue sarcomas (6–8). Given the lack of highly effective FDA-approved therapies for SS, the development of novel, targeted therapeutics is warranted.

Identification of metabolic alterations that arise in malignancies can lead to the development of new therapeutic targets. Overexpression of malic enzyme 1 (ME1) has been associated with more aggressive cancer phenotypes (9–15). In addition, increased ME1 expression has been demonstrated to be both a prognostic and a predictive marker for sensitivity to radiotherapy (14, 16–18). To date, a recurrent loss of ME1 expression has never been reported in any cancer. ME1 catalyzes the reversible oxidative decarboxylation of malate to pyruvate, yielding NADPH from $NADP^+$ (19–21). Several cytosolic enzymes, along with ME1, produce NADPH, includingglucose-6-phosphate dehydrogenase (G6PD) and 6-phosphogluconate dehydrogenase (6PGD) of the pentose phosphate pathway (oxPPP), as well as isocitrate dehydrogenases

[1]Division of Medical Oncology, Washington University in St. Louis, St. Louis, Missouri. [2]Department of Surgery, Washington University in St. Louis School of Medicine, St. Louis, Missouri. [3]Department of Pathology and Immunology, Division of Anatomic and Molecular Pathology, Washington University in St. Louis, St. Louis, Missouri. [4]Department of Molecular Physiology and Biophysics, Carver College of Medicine, University of Iowa, Iowa City, Iowa. [5]Department of Pathology and Laboratory Medicine, The University of British Columbia, Vancouver, British Columbia, Canada. [6]Departments of Melanoma Medical Oncology and Genomic Medicine, The University of Texas MD Anderson Cancer Center, Houston, Texas. [7]Siteman Cancer Center, Washington University in St. Louis, St. Louis, Missouri. [8]Department of Orthopedics, University of Utah, Salt Lake City, Utah. [9]Department of Oncological Sciences, University of Utah, Salt Lake City, Utah. [10]Huntsman Cancer Institute, University of Utah, Salt Lake City, Utah. [11]Department of Orthopedics, Washington University in St. Louis, St. Louis, Missouri. [12]Holden Comprehensive Cancer Center, University of Iowa, Iowa City, Iowa. [13]Fraternal Order of Eagles Diabetes Research Center, University of Iowa, Iowa City, Iowa. [14]Department of Anesthesiology, Washington University in St. Louis, St. Louis, Missouri. [15]Department of Pediatrics, Washington University in St. Louis, St. Louis, Missouri.

C.B. Brashears and B.C. Prudner share first authorship of this work.

Corresponding Author: Brian A. Van Tine, Division of Medical Oncology, Washington University in St. Louis, 660 South Euclid, Campus Box 8007, St. Louis, MO 63110. Phone: 314-747-3096: E-mail: bvantine@wustl.edu

Clin Cancer Res 2022;28:3573–89

doi: 10.1158/1078-0432.CCR-22-0470

Translational Relevance

Synovial sarcoma (SS) is the most common translocation-driven soft-tissue sarcoma. Although the driving gene fusion between *SS18* and the X chromosome is well characterized, there are currently no therapies that specifically target the innate biology of SS. Therefore, there is a need in the field for the development of targeted therapeutics. In this study, we have identified SS as the first cancer to exhibit a recurrent loss of malic enzyme 1 (ME1). The absence of ME1 in SS causes significant shifts in redox homeostasis that result in increased susceptibility to ferroptosis induction both *in vitro* and *in vivo*. These preclinical findings highlight the potential therapeutic applications for targeting redox homeostasis in ME1-null tumors as well as the potential translational efficacy of ferroptosis inducing agents, such as ACXT-3102.

(IDH; ref. 22). There are also enzymes in the one-carbon-tetrahydrofolate oxidation pathways that make a small contribution to the cytosolic NADPH pool (23–25). Flux through the ME1 pathway produces NADPH levels equivalent to that of enzymes within the oxPPP, implicating ME1 as a major cytoplasmic source of NADPH (26, 27).

NADPH is an important reducing equivalent, providing electrons for antioxidant defense and reductive biosynthesis. Cytosolic NADPH is used for redox metabolism in the glutathione and thioredoxin antioxidant pathways. These pathways allow cells to maintain reactive oxygen species (ROS) levels, which act as signaling molecules to support proliferation and survival (28). The highly proliferative state of cancer leads to an increases in ROS levels that can cause oxidative stress and potentially result in cell senescence or death (29, 30). Cancer cells compensate for increased ROS through the upregulation of antioxidant pathways, such as the glutathione or thioredoxin systems. When ROS accumulates above a threshold level, protein, lipid, and DNA oxidation can occur; therefore, the balance between ROS production and clearance is tightly regulated.

Both the thioredoxin pathway and glutathione pathway are disulfide reductase systems that control cellular redox homeostasis. The thioredoxin system is composed of thioredoxin (Trx), thioredoxin reductase (TrxR), and NADPH. Trx is important in reducing oxidized cysteine and cleaving disulfide bonds of surrounding proteins with a CXXC motif (31). The glutathione system is composed of the tripeptide glutathione (y-glutamyl–cyteinyl–glycine) in a reduced form (GSH) and an oxidized form (GSSG), as well as GSSG reductase (GR), glutathione peroxidase (GPX), glutaredoxins (Grx), and NADPH (32). Within the glutathione pathway, GPX uses GSH as a reducing equivalent to neutralize intracellular peroxides such as H_2O_2. As a result, when the glutathione pathway is hindered, H_2O_2 accumulates (33–35). *De novo* synthesis of both GSH and Trx requires the intermediate precursor cysteine. Cystine, the stable precursor, is imported via the cystine–glutamate exchanger xCT (SLC7A11). Intracellularly, cystine is reduced to cysteine, which provides the key antioxidant component of both GSH and Trx (36).

Inhibition or dysregulation of cysteine metabolism and/or cellular antioxidant systems can lead to ROS-mediated cell death processes, such as ferroptosis. Ferroptosis is a form of nonapoptotic cell death that is characterized by iron dependency and overwhelming lipid peroxidation (37, 38). xCT (SLC7A11) is a cystine–glutamate antiporter and the main mechanism of extracellular cystine import necessary for the maintenance of intracellular cysteine pools. Inhibition of xCT is a well-described mechanism of ferroptosis induction (37). Although upregulation of cysteine import and cellular antioxidant systems are features of cancer metabolism may protect from ferroptosis, the rewiring of iron metabolism in cancer can predispose to ferroptotic cell death (39). The upregulation of iron import and the expansion of the liable iron pool are features of cancer metabolism that potentiate ROS accumulation, through the iron-dependent Fenton reaction, and cell death through ferroptosis (39). Therefore, induction of ferroptosis has become an attractive target for the development cancer therapeutics.

In this study, profiling of metabolic genes was performed to identify possible metabolic vulnerabilities within SS. This revealed the first cancer, monophasic SS, that lacks expression of ME1. This study demonstrates that ME1 absence drives a unique innate redox system. The absence of ME1 expression in SS tumors results in a dependency upon the oxPPP for the production of cytoplasmic NADPH, an essential cellular antioxidant. Consistently, SS exhibits significant alterations in redox homeostasis, as SS is exquisitely sensitive to Trx inhibition, whereas activity of the glutathione pathway is reduced. Decreased glutathione pathway activity results in an increased concentration of intracellular H_2O_2. Concomitantly, ME1 absence drives increases in the free labile iron pools. The accumulation of cellular ROS and increases the labile iron pool result in increased sensitivity to ferroptosis induction. Enhanced sensitivity to ferroptosis can be exploited through inhibition of xCT by ACXT-3102 (Sigma-2/erastin) both *in vitro* and *in vivo*. Additionally, not only is disruption of redox homeostasis with xCT inhibition a valid translational target in SS, but the response of xCT inhibition in this context is dependent upon the ME1 expression status of the tumor. Taken together, disruption of the innate redox biology in ME1-null cells could be harnessed as a useful therapeutic target in SS.

Materials and Methods

Cell lines

The following human sarcoma cell lines were kindly provided: SK-LMS-1, MG-63, HTB-93 (ATCC), SYO-1 (Dr. Akira Kawai, National Cancer Centre Hospital, Tokyo, Japan), Fuji (Dr. Kazuo Nagashima, Hokkaido University School of Medicine, Sapporo, Japan), Aska-SS, Yamata-SS, HS-SY-II (purchased from Riken BRC, deposited by Dr. Naka Norifumi and Dr. Sonobe Hiroshi, Ibaraki, Japan), and MOJO (Dr. K. Jones, University of Utah, Salt Lake City, UT). SYO, Fuji, Aska-SS, Yamata-SS, MOJO, and HS-SY-II were authenticated by confirming expression of SYT–SSX fusion gene by RT-PCR. HTB-93 was isolated in 1974 morphologically resembles SS but lacks the pathognomonic translocation that is classic for SS, making it a tissue type control that does not represent translocation dependent SS biology (40). SK-LMS-1, MG-63, Aska-SS, HS-SY-II, HTB-93, MOJO, SYO-1, and Yamata-SS cell lines were cultured at 37°C in 5% CO_2, in Dulbecco's modified Eagle medium (Life Technologies) supplemented with 10% FBS and penicillin–streptomycin 100× (10,000U/mL) (Life Technologies) Fuji was cultured in RPMI Medium 1640 (Life Technologies) supplemented with 10% FBS and penicillin–streptomycin 100× (10,000U/mL) (Life Technologies). Cell lines were tested for *mycoplasma* monthly and confirmed negative with the MycoAlert Mycoplasma Detection kit (Lonza LT07-118). All cell lines were cultured for less than 6 months after thawing.

Microarray

Synovial sarcoma samples are from gene-expression omnibus (GEO) accession GSE20196 (41), and other sarcoma samples are from GSE21050 (42), GSE23980 (43), and GSE20559 (44). Baseline and insulin-sensitive cases were selected from studies involving subcutaneous abdominal fat (adipose) and/or vastus lateralis muscle (skeletal muscle), from accessions GSE13070 (45), GSE20950 (46), GSE13506 (47), GSE35411 (48), GSE6798 (49), and GSE18583 (50). Raw CEL files were downloaded from GEO and processed using BioConductor packages within the R statistical software environment (http://www.R-project.org) (51). Array quality was assessed using the package simpleaffy (52), and outlying arrays were identified and excluded using the package mdqc (53). Log base 2 expression values were determined using the package gcrma (54), with Affymetrix probe set specifications. Data were median centered, such that the expression value for each gene is relative to the median value across all specimens in the cohort.

IHC

Formalin-fixed paraffin-embedded slides were deparaffinized after incubation at 65°C for 1 hour, rehydrated, and incubated in 3% hydrogen peroxide for 10 minutes. Slides were heated in antigen unmasking solution (Vector). Primary antibody (1:100 malic enzyme 1, ab97445, Abcam) was applied to each slide and incubated overnight at 4°C. Biotinylated secondary antibody (1:100 goat anti-rabbit, BA-10a00, Vector Laboratories, Inc) was applied and incubated at room temperature for 30 to 40 minutes. After washing, ABC complex (Vector Laboratories, Inc) was applied and incubated for 30 minutes. DAB (Vector Laboratories, Inc) was then applied and allowed to incubate 30 to 60 minutes. Slides were then immediately counterstained with hematoxylin 1 (Thermo Fisher Scientific Inc) and mounted. IRB approval for the use of deidentified tissue samples was obtained from Washington University in St Louis.

qRT-PCR

RNA was collected from cell lines and tumor samples using NucleoSpin RNA/Protein Kit (740933, Machery-Nagel). cDNA was synthesized using the High-Capacity cDNA Reverse Transcriptase Kit (4368813, Applied Biosystems). Quantitative reverse transcription-PCR (qRT-PCR) was conducted using Power SYBR Green PCR Master Mix (4367659, Applied Biosystems) on a CFX96 Touch Real-Time PCR Detection System (Bio-Rad). Primers for qRT-PCR were purchased from Integrated DNA Technologies. Sequences for primers utilized were as follows: ME1, 5′-TCACCTCAACAAGGACTTGGC-3′ (forward primer), 5′-AAGTCAGAGTTCAGATGCTCG-3′ (reverse primer); human 18S rRNA, 5′-CTACCACATCCAAGGAAGCA-3′ (forward primer), and 5′-TTTTTCGTCACTACCTCCCCG-3′ (reverse primer). Cycling conditions were as follows: Step 1, 95°C for 10 minutes; step 2, 95°C for 15 seconds; step 3, 60°C for 60 seconds; repeat steps 2/3 39 times, for a total of 40 cycles. Quantification of ME1 expression was conducted using ΔΔCq, using human 18S rRNA as a housekeeping gene.

ME1 activity assay

Cells were plated at 1×10^6 in 10-cm dishes the day before the assay was performed. Cells were collected and a cytoplasmic fraction was produced (Cayman #10009277). The cytoplasmic fraction was then accessed according to the manufacturer's protocol (Pyruvate Assay Kit, ab65342; Abcam). This protocol was adapted by substituting the pyruvate enzyme mix with malate enzyme mix composed of 67 mmol/L triethanolamine, 3.3 mmol/L L-malate, 0.3 mmol/L β-$NADP^+$, and 5 mmol/L $MgCl_2$ (25, 55). All other steps within the manufacturer's protocol were followed.

Lentiviral-mediated ME1 expression

The ME1 overexpression vector ME1/pBABE-puro (Plasmid #49163) was purchased from Addgene as bacteria in an agar stab and subsequently transformed into competent XL10 bacteria and purified into plasmid DNA with Qiagen Plasmid Plus Midi Kit (12945Qiagen Inc). TransIT-LT1 Transfection reagent (Mirus) was used for plasmid transfection of retro-VSVG and pLECO, plasmid into Lenti-X 293T cells (Takara). Viral supernatants were harvested and cells were transduced at 40 MOI with viral particles. Transduced cells were selected for and maintained by culturing in puromycin. ME1 knockdown lentiviral particles (Mission shRNA: TRCN0000064730, TRCN0000064728, and TRCN0000064732) were purchased from Millipore-Sigma. For the vector control MISSON pLKO.1-puro Non-target shRNA control Transduction Particles were purchased from Millipore-Sigma (SHC016V). Cells were transduced and selected per manufacturer's protocol.

Immunoassays

For analysis of ME1 expression (sc-100569, Santa Cruz), cells were seeded at 3×10^5 in a 6-well plate 1 day prior to collection. On day of collection, media were removed, and cells were washed 3 times with 1× PBS. Cells were collected and lysed per reagent protocol of 1 Cell Lysis Buffer (9803, Cell Signaling Technology). Lysates were run on a ProteinSimple Wes Capillary electrophoresis instrument using instrument default settings and manufacturer's standard protocol. The antibodies and dilutions were as follows: ME1 1:50 (SAB4501853 Millipore-Sigma).

Seahorse assays

Both the Seahorse cell energy phenotype and fuel flex assays were performed per manufacturer's protocol (Agilent). Cells were seeded in a Seahorse 96-well plate: SYO and FUJI at 40,000/well and HTB-93 at 30,000/well 12 hours prior to assay. After performance of the Seahorse assay, cell counts were measured using YOYO-1 iodide (Y3601, Thermo Fisher Scientific Inc) on the IncuCyte Zoom live-cell imaging system and the Seahorse results were normalized to cell count.

Metabolomic assays

For whole metabolomic analysis, SYO-1 WT, Fuji WT, SYO-1 OE, and Fuji OE were plated at 1×10^6 cells in a 10-cm dish in MEM. Media were removed and replaced with fresh media containing 5 mmol/L glucose and 2 mmol/L labeled glutamine for 4 hours. After the incubation period, methanol metabolite extraction was performed according to HMT metabolite extraction protocol. Metabolome analysis was performed by HMT using CE-TOFMS.

For $U^{13}C$ glutamine tracings, SYO-1 WT, Fuji WT, SYO-1 OE, and Fuji OE were plated at 1×10^6 cells in a 10-cm dish in MEM. Media were removed and replaced with $U^{13}C$ glutamine (Cambridge Isotope Laboratories) media containing 5 mmol/L glucose and 2 mmol/L labeled glutamine for 2, 4, or 8 hours. After the incubation period, methanol metabolite extraction was performed according to the HMT metabolite extraction protocol. Metabolome analysis was performed by HMT using CE-TOFMS. The data were corrected for natural abundance of C^{13}.

For 1,2 ^{13}C glucose tracings, SYO-1 WT and SYO-1 OE were plated at 1×10^6 cells in a 10-cm dish in MEM. Three hours prior to application of the tracing media, plates were washed with PBS, and the media were refreshed with new MEM. Media were removed and

replaced with 1,2 ^{13}C glucose (Cambridge Isotope Laboratories) at 5 mmol/L and 4 mmol/L glutamine for 24 hours. After the incubation period, methanol metabolite extraction was performed according to the HMT metabolite extraction protocol. Metabolome analysis was performed by HMT using CE-TOFMS. The data were corrected for natural abundance of C^{13}.

NADPH measurements

SYO-WT, SYO-OE, HTB93-WT, and HTB93-KD3 cells were seeded at 3 million cells per 10-cm dish 1 day prior to collection. Samples were treated with physiologic glucose levels (5 mmol/L) or without glucose for 3 hours. On the day of collection samples were washed briefly with ice-cold sterile water twice. After two washes cells were flash frozen on the 10-cm dish in liquid nitrogen prior to extraction.

Extraction buffer was prepared by adding 2:2:1 methanol/acetonitrile/water, 0.1 M formic acid, and internal standards at 1 μg/mL each (D4-Citric Acid, 13C5-glutamine, 13C5-glutamic acid, 13C6-lysine, 13C5-methionine, 13C3-serine, D4-succinic acid, 13C11-tryptophan, and D8-valine; Cambridge Isotope Laboratories) to lyophilized cell samples. Cells were scraped for 20 seconds and collected into Eppendorf tubes, flash frozen in liquid nitrogen, and sonicated for 10 minutes. Samples were then placed on a rotating platform at –20°C for 1 hour and centrifuged at 4°C for 10 minutes at 21,000 × *g*. Cleared metabolite extracts (300 μL) was transferred to fresh tubes for additional processing. An equal volume of each extract was pooled to serve as a quality control (QC) sample, which was analyzed at the beginning, end, and at regular intervals throughout the instrument run. Extraction buffer alone was analyzed as a processing blank sample. Metabolite extracts, the QC sample, and the processing blank were evaporated to dryness using a speed vacuum.

For liquid chromatography mass spectrometry (LC-MS), the dried metabolite extracts, QC sample, and processing blank sample were reconstituted in 30 μL of acetonitrile/water (1:1, V/V), vortexed, and centrifuged at 4°C for 10 minutes at 21,000 × *g*. Samples were then placed on a rotating platform at –20°C for 2 hours and centrifuged at 4°C for 2 minutes at 21,000 × *g*. Samples were then transferred to autosampler vials for analysis.

For LC chromatographic separation, 2 μL of reconstituted metabolite extracts, QC sample, and processing blank were run on a Millipore SeQuant ZIC-pHILIC (2.1 × 150 mm, 5-μm particle size) column with a ZIC-pHILIC guard column (20 × 2.1 mm) attached to a Thermo Vanquish Flex UHPLC. Mobile phase comprised buffer A: 20 mmol/L $(NH_4)_2CO_3$, 0.1% NH_4OH and buffer B: acetonitrile. The chromatographic gradient was run at a flow rate of 0.150 mL/minute as follows: 0–21 minutes-linear gradient from 80% to 20% buffer B; 20 to 20.5 minutes-linear gradient from 20% to 80% buffer B; and 20.5–28 minutes-hold at 80% buffer B. Data were acquired using a Thermo Q Exactive MS operated in full-scan, polarity-switching mode with a spray voltage set to 3.0 kV, the heated capillary held at 275°C, and the HESI probe held at 350°C. The sheath gas flow was set to 40 units, the auxiliary gas flow was set to 15 units, and the sweep gas flow was set to 1 unit. MS data acquisition was performed in a range of $m/z = 70–1{,}000$, with the resolution set at 70,000, the AGC target at 10e6, and the maximum injection time at 200 ms.

TraceFinder 5.1 was utilized to identify metabolites based on *m*/*z* and retention times that were determined by an in-house library of standards. After attaining metabolite identification and peak area integration by TraceFinder, the NOREVA software (http://idrblab.cn/noreva2017) was used for signal drift correction on a metabolite-to-metabolite basis using multiple analyses of the QC sample throughout the instrument run. Metabolite peak intensities were then normalized to total ion signal.

Drug treatment and cell death assays

Nuclight Red cell lines were seeded at 20,000 cells in a 96-well plate (SYO-WT, SYO-OE, Fuji WT, Fuji OE, HTB-93-WT, and HTB-93-KDs) 1 day before assay. Cells were treated with either 25 μmol/L G6PDi-1 (72 hours), 2 mmol/L BSO (24 hours), 1.2 μmol/L D9 (12 hours), 250 μmol/L deferoxamine (5 hours), erastin (dosage indicated per cell line 48 hours), or 1 μmol/L ACXT-3102 (5 hours). For rescue of erastin treatment with lipophilic antioxidants or ferrostatin, the dosages were as follows: 200 μmol/L Trolox, 100 μmol/L a-tocopherol, and 10 μmol/L ferrostatin. Erastin rescue experiments were treated for 72 hours. Phenol red-free media containing drug concentration as well as 50 nmol/L of YOYO-1 iodide (Y3601, Thermo Fisher Scientific Inc) cell death marker replaced growth media. Cell death was measured via the YOYO-1 iodide probe, and live-cell analysis was measured using Nuclight Red (4717, Sartorius). Cell death was analyzed using IncuCyte FLR imaging system software (Sartorius). For quantification of death, YOYO-1 florescence was normalized to total counts for each respective well. The drugs utilized in these experiments were obtained as follows: BSO (14484, Cayman Chemical), D9 (5921, Tocris), deferoxamine (S5742, Selleckchem), Trolox (93510, Millipore-Sigma), a-tocopherol (1667600, Millipore-Sigma), and ferrostatin (S7243, Selleckchem).

Iron and hydrogen peroxide assay

Nuclight Red cell lines were seeded at 20,000/well (SYO WT, SYO-OE, FUJI WT, and FUIJI OE) in a 96-well plate. Cell lines were incubated with each probe per the manufacturer's protocol. Fe^{3+} (Ferrum 430, Ursa BioScience), Fe^{2+} (FeRhoNox-1, Goryo Chemical), and H_2O_2 (HYDROP, Goryo Chemical). Wells were imaged every 15 minutes over 1 hour, and analyzed using IncuCyte image analysis software (Sartorius). Probe excitation was quantified using and IncuCyte FLR imaging system (Sartorius).

Lipid peroxidation assay

Cells were plated at 10,000 cells/well (SYO-1 WT, SYO-1 ME1 OE, Fuji WT, Fuji ME1 OE, HTB93 WT, and HTB93 KDs) the day before treatment with erastin. Cells were treated with erastin (1 μmol/L, 4 μmol/L, or 8 μmol/L) and incubated for 18 hours at 37∘C. After incubation, the media were removed, and cells were treated with 10 μmol/L Image-IT (Invitrogen C10445) for 30 minutes. Cells were washed with PBS, and fluorescence was then measured on the plate reader (Ex/Em: 488/510 nm). After completion of fluorescent measurement, cell counts were measured using YOYO-1 on the IncuCyte S3 live-cell imaging system, and the fluorescent measurements were normalized to cell count.

In vivo drug treatment

All animal experiments were under an approved protocol at Washington University. Animal care followed Institutional Animal Care and Use Committee standards.

ACXT-3102: Six- to seven-week-old athymic nu/nu female mice were obtained from The Jackson Laboratories (Nu/J homozygous cat. #002019). Mice were maintained at 5 animals per cage under humidity and temperature-controlled conditions in a light/dark cycle that was set at 12-hour intervals. Mice were injected subcutaneously in the right flank with a suspension of 1×10^6 SYO-1 WT ME1-null or 1×10^6 SYO-1 ME1 OE cells in an equal volume of Matrigel (Fisher Scientific). Total volume was approximately 0.1 mL. Tumors were measured in

two dimensions with a digital caliper (Model 15077958, Fisher Scientific, Intl), and tumor volumes were calculated by the standard formula of tumor volume = length × width squared × 0.5. Treatments began when mean tumor volume reached 200 mm^3. Animals were randomly assigned to control group (WT ME1-null $n = 10$, ME1 OE $n = 10$) or compound ACXT-3102–treated group (WT ME1-null $n = 10$, ME1 OE $n = 10$). Controls received oral doses of the vehicle: normal saline. ACXT-3102 was given orally at 60 mg/kg daily. Body weights were obtained prior to dosing each day, and the dose of the compound was adjusted accordingly. Mice were sacrificed when tumors reached 2 cm^3 or had ulcerated.

Statistical analysis

Data were analyzed using GraphPad Prism 7 Software. *In vitro* protein expression, cell death, activity assay, uptake assays, lipid peroxidation, and labile iron data are expressed as mean ± standard deviation and Student *t* test for the individual group comparison. Statistical analysis for *in vivo* study data was performed by analysis of variance for multiple-group comparison and two-way ANOVA for the individual group comparison with data expressed as standard error of the mean. $^{*}, P < 0.05$; $^{**}, P < 0.01$; $^{***}, P < 0.001$; $^{****}, P < 0.0001$ were considered to represent statistically significant group differences.

Data availability

For the RNA microarray, we used publicly available data sets from GEO accession. For detailed description of data accession, refer to the methods. The raw data files for the metabolomics analyses are available as extended data tables. For access to other raw data files associated with figures within this paper, please contact the corresponding author. For access to the xCT inhibitor ACXT-3102 contact Accuronix Therapeutics (https://accuronix.com/contact/).

Results

Synovial sarcoma lacks malic enzyme 1 expression

mRNA microarray analysis of a variety of metabolic enzymes in human tumor samples was conducted to identify metabolic vulnerabilities in SS. The microarray revealed a relative loss of *ME1* expression specifically in SS samples (**Fig. 1A**). ME1 protein expression was analyzed by IHC in human tumor samples, including 20 SS and 20 leiomyosarcoma (LMS) patient tissue samples (**Fig. 1B–E**). Samples were scored based on proportion of ME1-positive cells (0–3) and the intensity of ME1 staining (0–3; Supplementary Fig. S1A–S1C). Prior to scoring, the 20 SS patient tumors were stratified into their pathologic classifications: monophasic (purely sarcoma), poorly differentiated, and biphasic (containing epithelioid and sarcomatous regions). Of the 10 monophasic SS samples, five samples stained completely negative for ME1 expression (**Fig. 1B**; Supplementary Fig. S1a–S1c), whereas eight samples demonstrated limited, sporadic staining in individual cells (**Fig. 1C**; Supplementary Fig. S1a–S1c). The poorly differentiated SS samples exhibited positive staining for ME1. Interestingly, in all 7 biphasic tumor samples, the mesenchymal portion of the tumor lacked ME1 expression, whereas the epithelial portion of the same tumor exhibited stronger ME1 expression (**Fig. 1D**; Supplementary Fig. S1a–S1c). The 20 LMS samples were all found to be positive for ME1 expression (**Fig. 1E**; Supplementary Fig. S1a–S1c). Finally, the quantified scoring values for monophasic SS and the spindled component of biphasic SS were each significantly lower than the LMS samples (Supplementary Fig. S1c).

To further confirm the absence of ME1 expression within other SS models, mRNA and protein expression was analyzed in transgenic SS18–SSX mouse tumor samples and in established SS cell lines (56, 57). Twenty-one samples were analyzed for mRNA expression: 18 synovial sarcoma samples (9 SSX1 and 9 SSX2 fusion cases) compared with three nontranslocation associated samples (mesenchymal stem cells, MG-63, and SK-LMS-1). All synovial sarcoma samples lacked mRNA expression of *ME1*, whereas the nontranslocation samples all exhibited *ME1* mRNA expression (**Fig. 1F**). Additionally, the TCGA database was queried for mRNA transcript levels of *ME1* in a cohort of SS, dedifferentiated liposarcoma (DDLPS), LMS, myxofibrosarcoma (MYXO), and undifferentiated pleomorphic sarcoma (UPS; ref. 58). SS was the only sarcoma of this cohort that exhibited significantly lower mRNA expression of *ME1* when compared with the other sarcoma subtypes (Supplementary Fig. S2). Finally, methylation-specific PCR was performed to investigate the mechanism of *ME1* mRNA-null expression. Methylation status of the *ME1* promoter was compared in MG-63 (osteosarcoma), SK-LMS-1 (LMS), and two SS cell lines (SYO-1 and Fuji; Supplementary Fig. S3). These data demonstrated significant methylation of the *ME1* promoter in cell lines that lack expression of *ME1* (SYO-1 and Fuji), but not in cells that express *ME1* (Supplementary Fig. S3).

To correlate protein expression with mRNA levels, ME1 expression in six synovial sarcoma cell lines (SYO-1, Fuji, MOJO, Yamata-SS, Aska-SS, and HS-SY-II) was compared with ME1 expression in two sarcoma cell lines (MG-63 and SK-LMS-1) and an SS cell line that lacks the pathognomonic t(X;18) translocation (HTB-93; **Fig. 1G**). All translocation-containing SS cell lines did not have ME1 expression as compared with MG-63, SK-LMS-1, and HTB-93 (**Fig. 1G**). Furthermore, samples lacking ME1 expression showed no ME1 enzyme activity, whereas samples with confirmed ME1 expression demonstrated strong enzymatic activity (**Fig. 1H**). The known, relevant genetics for each cell line are included in Supplementary Table S1.

Recently, Barrot and colleagues proposed a novel cell of origin for SS, the periosteal progenitor cell (1). Due to this finding, we hypothesized that the ME1-null expression could be inherited from this proposed cell of origin. Using three independent human periosteal cell lysates and a mouse model of synovial sarcoma derived from periosteal progenitor cells ($n = 7$) *in vivo*, we demonstrated that ME1 is not expressed in the proposed cell lineage of origin (**Fig. 1I**).

Taken together, these data demonstrate that the absence of ME1 expression is consistent across multiple sample sets of SS human cell lines, SS tissue samples, and tumors from SS transgenic mouse models. Furthermore, ME1-null expression likely originates from the cell of origin, suggesting that ME1 absence is the innate biology of the hypothesized periosteal progenitor cells from which SS is derived.

Lack of malic enzyme 1 favors a glycolytic phenotype with concomitant upregulation of the oxPPP in SS

Previous studies have demonstrated that ME1 knockdown cells are sensitized to rapid cell death with glucose withdrawal (59). To determine if this phenotype is similar in tumors that innately lack ME1 expression, the two major energy-producing pathways, glycolysis and oxidative phosphorylation (OXPHOS), were measured using an energy phenotype assay in ME1-null cell lines (HS-SY-II WT, SYO-1 WT, and Fuji WT) and in isogenic ME1-overexpression cell lines (HS-SY-II OE, SYO-1 OE, and Fuji OE; Supplementary Fig. S4a and S4b). Comparing oxygen consumption rate (OCAR) with the extracellular acidification rate (ECAR) gives an understanding of the energetic phenotype in cells. WT ME1-null cell lines were found to have a less energetic phenotype than cell lines that express ME1 (ME1-OE; **Fig. 2A**; Supplementary Fig. S5). In contrast, the opposite phenotype was found in ME1-knockdown (ME1-KD) cells, where

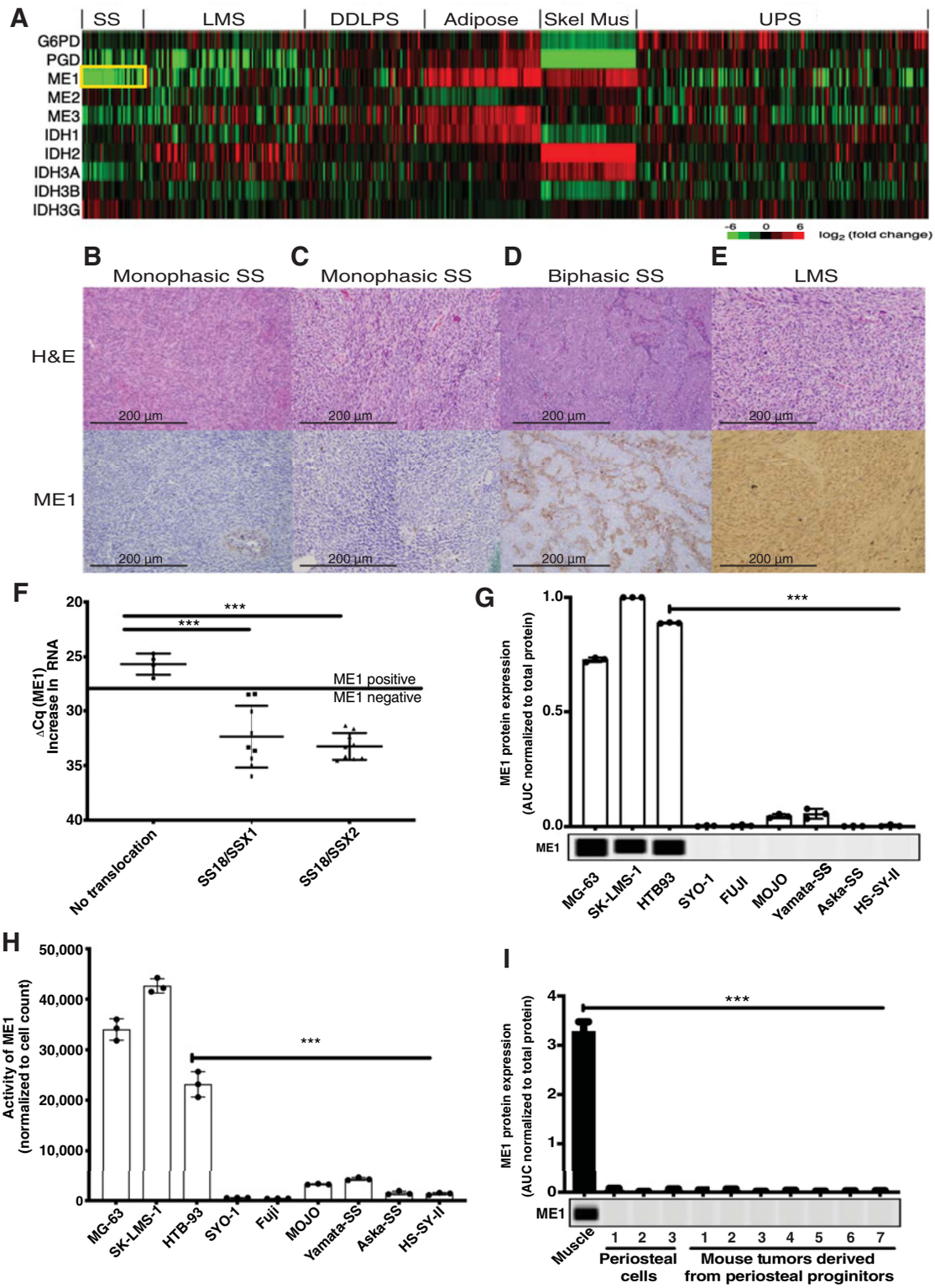
A
SS
LMS
DDLPS
Adipose
Skel Mus
UPS
G6PD
PGD
ME1
ME2
ME3
IDH1
IDH2
IDH3A
IDH3B
IDH3G
-6
0
6
log2 (fold change)
B
Monophasic SS
C
Monophasic SS
D
Biphasic SS
E
LMS
H&E
ME1
200 μm
F
ΔCq (ME1)
Increase in RNA
ME1 positive
ME1 negative
***
***
No translocation
SS18/SSX1
SS18/SSX2
G
ME1 protein expression
(AUC normalized to total protein)
***
ME1
MG-63
SK-LMS-1
HTB93
SYO-1
FUJI
MOJO
Yamata-SS
Aska-SS
HS-SY-II
H
Activity of ME1
(normalized to cell count)
***
MG-63
SK-LMS-1
HTB-93
SYO-1
Fuji
MOJO
Yamata-SS
Aska-SS
HS-SY-II
I
ME1 protein expression
(AUC normalized to total protein)
***
ME1
Muscle
Periosteal cells
Mouse tumors derived from periosteal proginitors

ME1 knockdown in HTB-93 cells caused a decrease in energetic phenotype (**Fig. 2B**; Supplementary Fig. S5). These data suggest that ME1-null cells are more glycolytic than oxidative.

In order to better understand the underlying metabolic alterations that lead to a less energetic phenotype in ME1-null cells, additional Seahorse assays were performed to specifically evaluate changes in glycolysis and OXPHOS. A glycolytic rate assay was performed to compare the rate of glycolysis in cells that lack ME1 and ME1-OE cells, which demonstrated that WT ME1-null cells are significantly more glycolytic than ME1-OE cells (**Fig. 2C**; refs. 60, 61). This led to the hypothesis that the reduced OCAR reliance in WT cells could be due to reduced glucose oxidation in the context of ME1 absence. To test this hypothesis, we performed a fuel flex assay, which demonstrated that WT ME1-null cells do not oxidize glucose when compared with ME1-OE cells (**Fig. 2D**). These data indicate that in ME1-null cells, the glucose that is shunted through glycolysis and is not oxidized through the mitochondria (**Fig. 2C** and **D**).

Because WT cells preferentially utilize glucose in glycolysis instead of shunting it to the mitochondria for OXPHOS, a global metabolite profile on SS WT ME1-null and ME1-OE cell lines was performed (Supplementary Table S2). The analysis demonstrated significant differences in oxPPP pathway metabolites between WT and OE cell lines. The amount of total beginning substrates within this pathway (glucose-6-phosphate and 6-phosphogluconic acid) do not change between WT ME1-null and ME1 OE cell lines (**Figs. 2E** and **F**), but the later substrates (ribulose-5-phosphate and ribose-5-phosphate) are increased significantly in WT ME1-null cell lines relative to ME1-OE cell lines (**Fig. 2G** and **H**). Similarly, unbiased pathway analysis of the global metabolite profile revealed statistically significant changes in the PPP in SYO-1 and Fuji WT ME1-null relative to ME1-OE cells (Supplementary Fig. S6a–S6b). To examine the functionality of the enzymes within the oxPPP pathway, the activity of G6PD and 6PGD, the two main NADPH-producing enzymes, was assessed. Based on these assays, activity of G6PD and 6PGD did not change in the context of ME1-OE (Supplementary Fig. S7a and S7b).

Although accumulation of downstream substrates may indicate increased flux through the oxPPP, it may alternatively suggest reduced flux through downstream pathways. It was hypothesized that the WT ME1-null cells have increased flux through the oxPPP relative to ME1-OE cells. In order to more definitively test this hypothesis, a 1,2-^{13}Cglucose tracing experiment was performed (62). 1,2-^{13}Cglucose that fluxes through glycolysis produces m+2 labeled lactate, whereas 1,2-^{13}C glucose that fluxes through the PPP produces m+1 labeled lactate. Comparison of the proportion of m+2 lactate with m+1 lactate produced a relative flux estimate of glucose flux through the PPP (**Fig. 2I**; ref. 62). WT ME1-null cells exhibit significantly higher ratios of m+1/m+2 lactate relative to ME1-OE cells, suggesting increased oxPPP flux in the absence of ME1 (**Fig. 2J**). Additionally, mass isotopomer distributions and abundance of downstream products of nucleic acid synthesis demonstrate that steady-state levels are equivalent in WT ME1-null and ME1-OE cells, indicating that the noted change in lactate labeling is not attributable to alterations in nucleotide synthesis (Supplementary Fig. S8). Altogether, these data indicate that cells that lack expression of ME1 exhibit reduced glucose oxidation and increased flux of glucose through glycolysis and the oxPPP.

G6PD inhibition leads to cell death in ME1-null SS

Glucose shunted to the oxPPP in ME1-null cells allows for NADPH to be generated even in the absence of ME1 (63). Due to differential glucose utilization in SS WT ME1-null as compared with ME1-OE cell lines, NADPH abundance was analyzed in 5 mmol/L glucose and glucose withdrawal conditions. In the SYO-1 WT ME1-null cell line, when glucose is withdrawn, intracellular levels of NADPH are significantly depleted relative to NADPH levels in 5 mmol/L glucose media (**Fig. 3A**). In contrast, in the SYO-1 ME1 OE cell line, glucose withdrawal did not result in significant reductions in the intracellular levels of NADPH (**Fig. 3A**). Additionally, in the ME1-expressing cell line HTB-93 glucose withdrawal resulted in a statistically significant reduction in NADPH levels (**Fig. 3B**). Whereas knockdown of ME1 in HTB-93 resulted in an enhanced reduction of NADPH levels in the presence of glucose withdrawal (**Fig. 3B**).

To exploit the reliance of WT ME1-null cells on the oxPPP, G6PD was pharmacologically inhibited by G6PDi-1, a novel, noncompetitive, allosteric inhibitor of G6PD (64). Inhibiting G6PD resulted in a significant induction of cell death in SYO-1 WT ME1-null cells, whereas ME1 expression provided significant protection from cell death (**Fig. 3C**). Similarly, ME1-expressing HTB-93 WT cells exhibited significantly less cell death with inhibition of G6PD compared with the HTB-93 ME1 KD cell lines (**Fig. 3D**). These results further support the hypothesis that WT ME1-null cells rely on the oxPPP for NADPH production and survival.

ME1 absence in SS results in altered redox homeostasis and iron redox status

NADPH is an essential cofactor in the recycling of redox antioxidant systems. Because NADPH production appears to be shifted to the oxPPP in WT ME1-null cells, metabolic analysis was performed to identify if this shift could affect levels of GSH and GSSG. Analysis of SYO-1 WT ME1-null and Fuji WT ME1-null global metabolite profiles revealed notable differences in the GSH and GSSG pools relative to SYO-1 ME1 OE and Fuji ME1 OE. Comparing GSH to GSSG in WT ME1-null versus ME1 OE SS cell lines, the total amount of GSH is much lower in WT ME1-null cells relative to ME1 OE cells (**Fig. 4A top**), whereas total levels of GSSG remained unchanged between the two groups (**Fig. 4A**, bottom). To investigate the mechanism

Figure 1.

SS lacks malic enzyme 1 expression. **A,** RNA microarray of metabolic enzymes in human tissue samples including SS, LMS, DDLPS, normal adipose tissue (adipose), normal skeletal muscle (Skel Mus), and UPS. **B,** Representative images of 20 SS and 20 LMS patient samples stained with hematoxylin and eosin (top) and anti-ME1 counterstained with hematoxylin (bottom), including (**B**) representative image of monophasic SS with conventional histology; (**C**) representative image of monophasic SS exhibiting limited, sporadic anti-ME1 staining; (**D**) representative image of biphasic SS; and **(E**) representative image of LMS, which served as a positive control for anti-ME1. **F,** qRT-PCR of ME1 in 21 sarcoma samples: 3 nontranslocation samples, 9 SS18:SSX1 SS samples, and 9 SS18:SSX2 SS samples. ***, $P < 0.001$. **G,** Protein expression of ME1 in osteosarcoma (MG-63), leiomyosarcoma (SK-LMS-1), and 7 SS cell lines (HTB-93, SYO-1, Fuji, MOJO, Yamata-SS, Aska-SS, and HS-SY-II). Cell lysates were analyzed with the Simple Protein Wes system. Band density differences were plotted as ME1 area under the curve normalized to total protein in the capillary (representative $n = 3$). Data are represented as mean ± SD; ***, $P < 0.001$. **H,** Enzymatic activity of ME1 in osteosarcoma (MG-63), leiomyosarcoma (SK-LMS-1), and SS cell lines (HTB-93, SYO-1, Fuji, MOJO, Yamata-SS, Aska-SS, and HS-SY-II). Data are represented as mean ± SD ($n = 3$); ***, $P < 0.001$. **I,** Protein expression of ME1 in periosteal cell lysates ($n = 3$) and tumors from SSX:SS18 spontaneous mouse tumors ($n = 7$). Mouse muscle tissue was used as positive control. Cell lysates were analyzed with the Simple Protein Wes system. Band density differences were plotted as ME1 area under the curve normalized to total protein in the capillary. Data, mean ± SD; ***, $P < 0.001$.

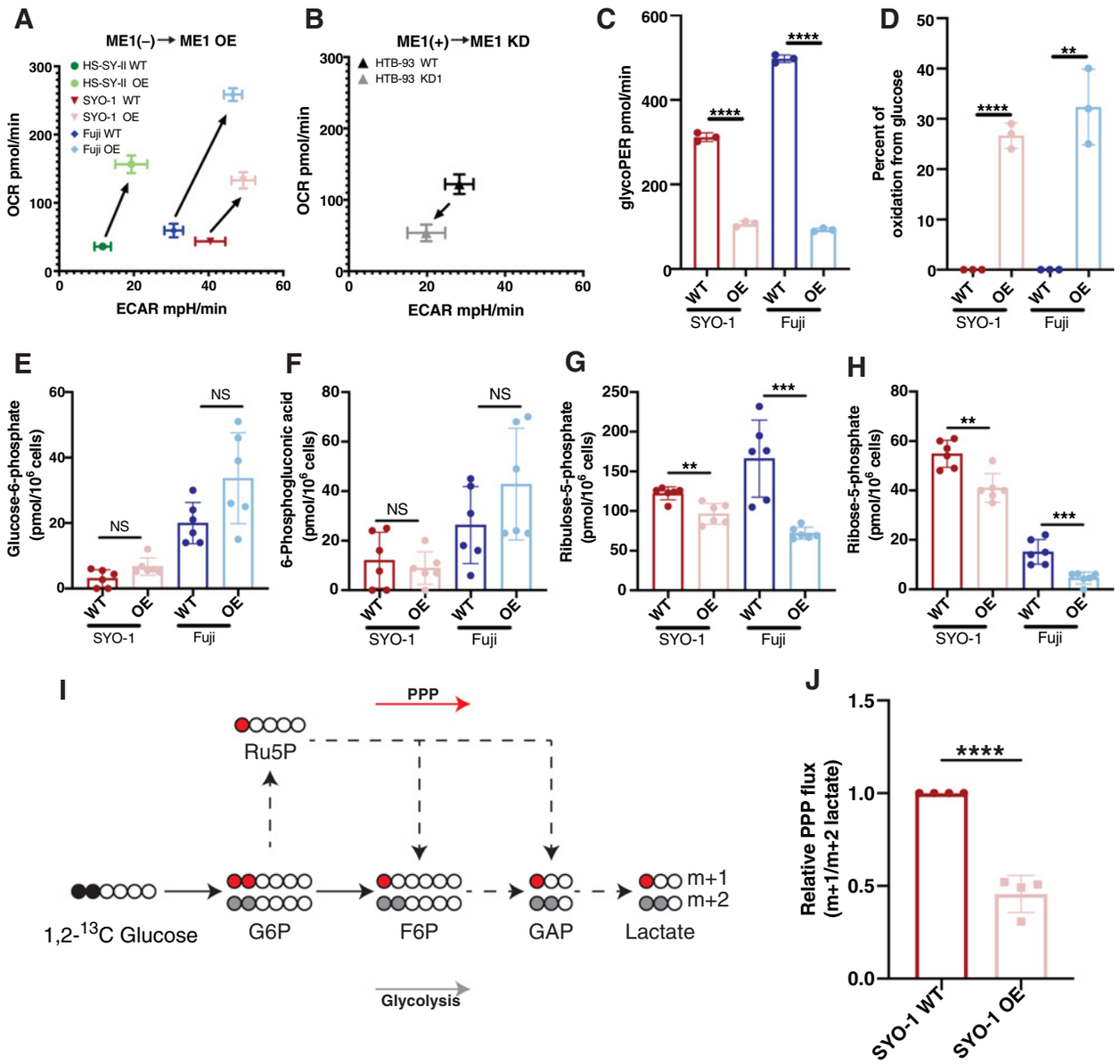

Figure 2.

Lack of malic enzyme 1 favors a glycolytic phenotype with concomitant upregulation of oxPPP in SS. **A,** Cell energy phenotype of ECAR vs. oxygen consumption rate (OCR) in ME1-null SS cell lines (SYO-1 WT, Fuji WT, HS-SY-II WT) and ME1 overexpression cell lines (SYO-1 OE, Fuji OE, HS-SY-II OE). Data, mean ± SD ($n = 3$). Arrows indicate direction of change upon ME1 overexpression. **B,** Cell energy phenotype of ECAR vs. OCR in ME1-expressing SS (HTB-93 WT) and ME1 knockdown cell line (HTB-93 KD1). Data, mean ± SD ($n = 3$). Arrows indicate direction of change upon ME1 knockdown. **C,** Glycolytic rate assay in ME1-null SS cell lines (SYO-1 WT and Fuji WT) and ME1 overexpression cell lines (SYO-1 OE and Fuji OE). Data, mean ± SD ($n = 3$); ****, $P < 0.0001$. **D,** Mitochondrial fuel flex assay showing the percentage of oxygen consumption from glucose fuel source in ME1-null SS cell lines (SYO-1 WT and Fuji WT) and ME1 overexpression cell lines (SYO-1 OE and Fuji OE). Data, mean ± SD ($n = 3$); ****, $P < 0.0001$; **, $P < 0.01$. **E,** Metabolite levels (pmol/10^6 cells) of upper pentose phosphate metabolite glucose-6-phosphate in ME1-null SS cell lines (SYO-1 WT and Fuji WT) and ME1 overexpression cell lines (SYO-1 OE, Fuji OE). Data, mean ± SD ($n = 6$); NS, $P > 0.5$. **F,** Metabolite levels (pmol/10^6 cells) of upper pentose phosphate metabolite 6-phosphogluconic acid in ME1-null SS cell lines (SYO-1 WT, Fuji WT) and ME1 overexpression cell lines (SYO-1 OE and Fuji OE). Data, mean ± SD ($n = 6$); NS, $P > 0.5$. **G,** Metabolite levels (pmol/10_6 cells) of lower pentose phosphate metabolite ribulose-5-phosphate in ME1-null SS cell lines (SYO-1 WT and Fuji WT) and ME1 overexpression cell lines (SYO-1 OE, Fuji OE). Data are represented as mean ± SD ($n = 6$); **, $P < 0.01$; ***$P < 0.001$. **H,** Metabolite levels (pmol/10^6 cells) of lower pentose phosphate metabolite ribose-5-phosphate in ME1-null SS cell lines (SYO-1 WT and Fuji WT) and ME1 overexpression cell lines (SYO-1 OE and Fuji OE). Data, mean ± SD ($n = 6$); **, $P < 0.01$; ***, $P < 0.001$. **I,** Tracing diagram depicting 1,2-^{13}C glucose labeling of substrates in glycolysis and PPP to produce m + 1 and m + 2 labeled lactate. **J,** Fraction of m + 1/m + 2 lactate from 1,2-^{13}C glucose in SYO-1 WT compared with SYO-1 OE. Data, mean ± SD ($n = 4$); ****, $P < 0.0001$.

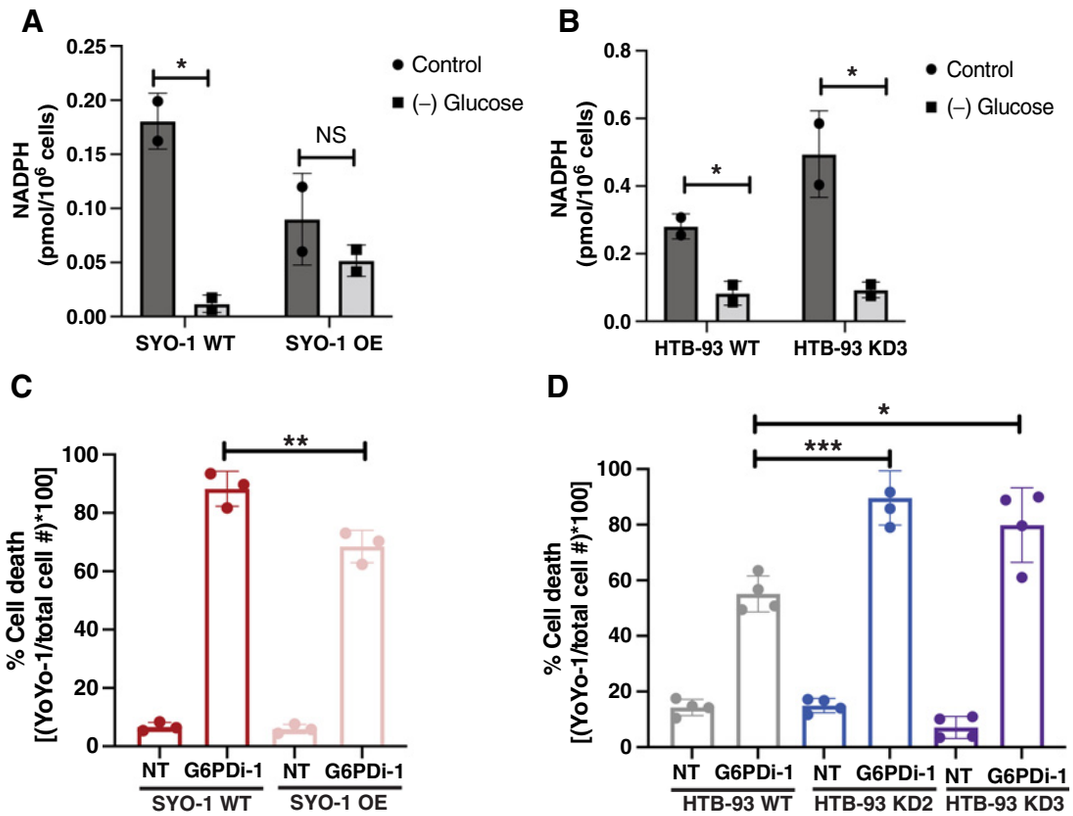

Figure 3.

G6PD inhibition leads to cell death in ME1-null SS. **A,** NADPH levels in SYO-1 WT ME1-null and SYO-1 ME1 OE in the presence of glucose (+) and under glucose withdrawal (−). Data, mean ± SD ($n = 3$); *, $P < 0.05$; NS, $P > 0.05$. **B,** NADPH levels in HTB-93 WT and HTB-93 ME1 KD3 in the presence of glucose (+) and under glucose withdrawal (−). Data, mean ± SD ($n = 3$); *, $P < 0.05$. **C,** *In vitro* cell death response to G6PDi-1 inhibition of glucose-6-phosphate dehydrogenase in SYO-1 WT ME1-null and SYO-1 ME1 OE. Data, mean ± SD ($n = 3$); **, $P < 0.01$. **D,** *In vitro* cell death response to G6PDi-1 inhibition of glucose-6-phosphate dehydrogenase in HTB-93 WT, HTB-93 ME1 KD2, and HTB-93 ME1 KD3. Data, mean ± SD ($n = 4$); *, $P < 0.01$; ***, $P < 0.001$.

underlying the change in total GSH levels, a universal glutamine tracer was utilized to evaluate GSH synthesis from glutamine and turn over into GSSG. The percent of glutamine labeled GSH and GSSG in the total pool, denoted by m + 10, m + 5, or m + other labeling, was compared in SS WT ME1-null and SS ME1 OE cell lines. The percent of labeled GSH in SYO-1 (**Fig. 4B, top**) and Fuji (**Fig. 4C, top**) within the total pool was less in WT ME1-null cells relative to ME1 OE cells. Additionally, the accumulation of glutamine incorporation over 2, 4, and 8 hours is higher in ME1-OE cells when compared with WT ME1-null cells, suggesting increased rates of GSH synthesis from glutamine. Similarly, total glutamine labeling of GSSG in SYO-1 (**Fig. 4B**, bottom) and Fuji (**Fig. 4C**, bottom) was reduced in WT ME1-null cells relative to ME1 OE cells (Supplementary Table S3). However, no conclusions can be drawn regarding the rate of GSH to GSSG turn over from this tracing experiment. Taken together, these data demonstrate that SS with an innate biology lacking ME1 expression exhibits significant reductions in their total GSH levels and likely reduced *de novo* synthesis of GSH from glutamine.

Due to the altered pools of GSH, it was hypothesized that treating SS with buthionine sulphoximine (BSO), an inhibitor of gamma-glutamylcysteine ligase, would induce death by further disrupting the glutathione pathway. Contrary to this hypothesis, treatment with BSO only induced significant cell death in ME1-expressing cell lines (**Fig. 4D**; Supplementary Fig. S9a). Treatment of transfection control cell lines with BSO confirmed that the change in sensitivity was due to ME1 expression and was unrelated to the vector (Supplementary Fig. S9b–S9c). Due to this unexpected result, overall thiol amounts were evaluated upon BSO treatment. Thiol amounts indicated that with BSO treatment WT ME1-null cells were more capable of increasing the overall abundance of thiols when compared with ME1-OE cells (**Fig. 4E** and **F**). Furthermore, on target activity of BSO was confirmed utilizing GSH-specific fluorescent probes. These data demonstrated that treatment with BSO resulted in significant reductions in cytoplasmic GSH (Supplementary Fig. S10). From these data it was hypothesized that an increase in overall thiol amount could be related to the thioredoxin antioxidant system. To evaluate the thioredoxin system, we compared sensitivity to a potent thioredoxin inhibitor (D9) in SS WT ME1-null and SS ME1 OE (65). D9 treatment induced significant levels of cell death in WT ME1-null cell lines and not in ME1 OE cell lines (**Fig. 4G**). Similarly, ME1 KD cell lines (HTB-93 KD) exhibited significantly increased cell death with D9 inhibition of thioredoxin reductase compared with ME1-expressing cell line HTB-93 (**Fig. 4G**; Supplementary Fig. S9d). Treatment of vector control cell lines with D9 confirmed that the change in sensitivity was due to ME1 expression changes and not a result of the vector (Supplementary Fig. S9e–S9f).Taken together, these results demonstrate a shift in redox homeostasis in the absence of ME1 expression

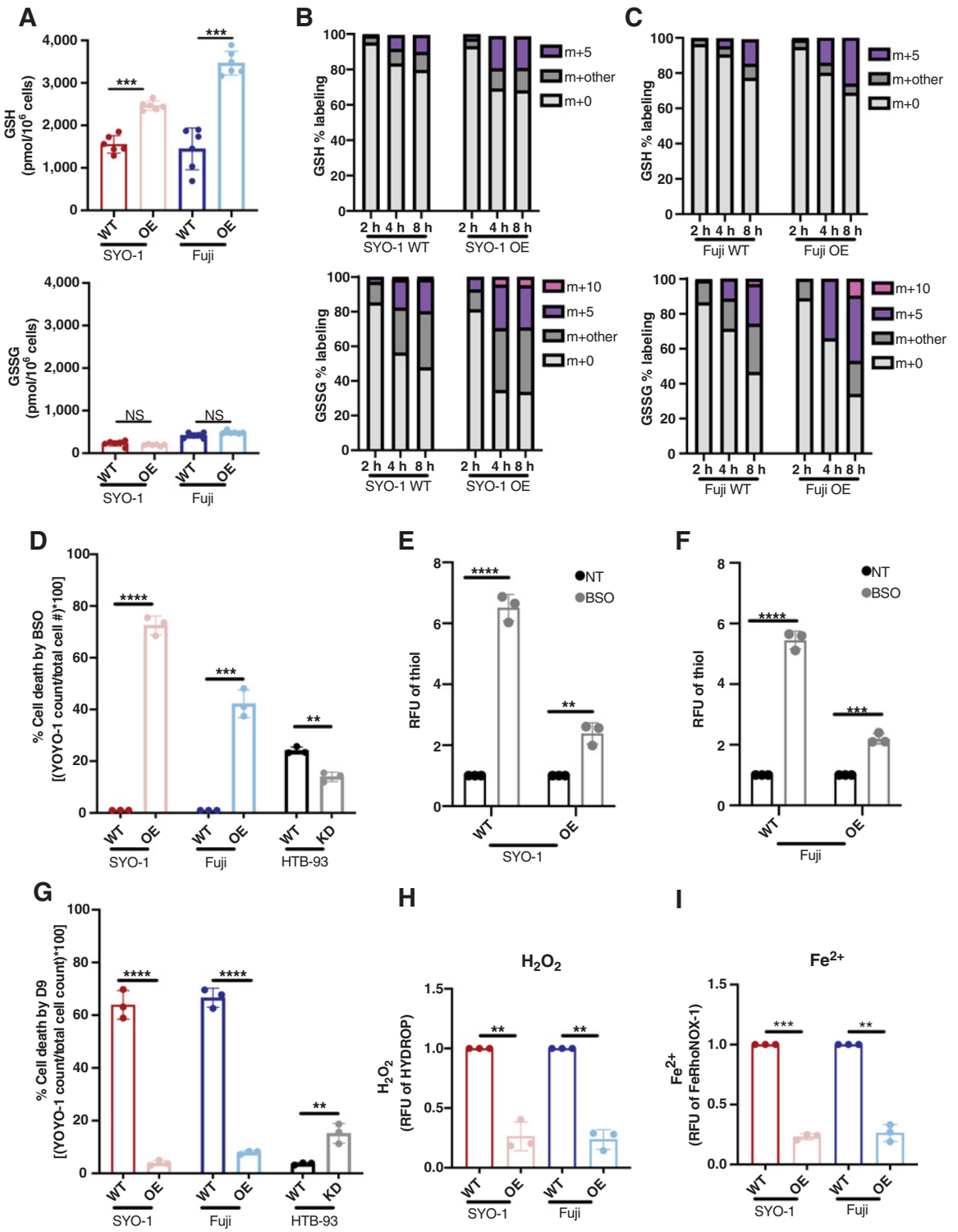

Figure 4.

ME1 absence in SS results in altered redox homeostasis and iron redox status. **A,** Metabolite levels (pmol/10^6 cells) of reduced glutathione (GSH; top) and oxidized glutathione (GSSG; bottom) in ME1-null SS cell lines (SYO-1 WT and Fuji WT) and ME1-overexpressing cell lines (SYO-1 OE and Fuji OE). Data, mean ± SD ($n = 6$); ***, $P < 0.001$. **B,** Average normalized isotopomer abundance from stable isotope tracing of $U^{13}C$-glutamine in reduced glutathione (GSH; top) and oxidized glutathione (GSSG; bottom) over time in ME1-null SS cell line SYO-1 WT and ME1-overexpressing cell line SYO-1 OE. Isotopomer abundance was normalized to cell count. (*Continued on the following page.*)

in SS. Specifically, the overall activity of the glutathione antioxidant system is reduced and sensitivity to inhibition of gamma-glutamylcysteine ligase is reduced, whereas sensitivity to inhibition of the thioredoxin system is increased in the absence of ME1. These data suggest that in the absence of ME1 expression in SS, the thioredoxin pathway is more essential for the maintenance of redox homeostasis than the glutathione pathway (**Fig. 4G**).

Due to the shift from glutathione to thioredoxin sensitivity, the impact on ROS levels was assessed, specifically H_2O_2. The glutathione antioxidant pathway plays a large role in managing H_2O_2, primarily through supporting the activity of glutathione peroxidases (32, 66). Therefore, a fluorescent probe was used to evaluate differences in baseline levels of H_2O_2 between WT ME1-null and ME1 OE cell lines. Consistent with reduced glutathione pathway activity, these data demonstrated that WT ME1-null SS cell lines have an increased level of intracellular H_2O_2 when compared with ME1 OE cell lines at baseline (**Fig. 4H**). It was hypothesized that the Fenton reaction, a pathway that depends upon H_2O_2 levels and free iron levels, would have increased flux as a result of the increased H_2O_2 burden (67). Essential components of the Fenton reaction were examined by baseline measurements of Fe^{2+} and Fe^{3+} (**Fig. 4I**; Supplementary Fig. S11). At baseline, WT cells have increased levels of Fe^{2+} compared with ME1-OE cells (**Fig. 4I**), whereas relative levels of Fe^{3+} are equivalent (Supplementary Fig. S11). Taken together, increased intracellular H_2O_2 levels and elevations in labile Fe^{2+} suggest increased potential for ROS production by the Fenton reaction (67). Collectively, these data indicate complex shifts in redox homeostasis in the context of ME1 absence, such that the dependency upon the thioredoxin pathway is enhanced whereas activity of the glutathione pathway is substantially reduced. Reductions in glutathione pathway activity are also evidenced in elevated levels of H_2O_2. These changes, combined with concomitant increases in the labile iron pool, suggested enhanced susceptibility to oxidative stress in cells that lack ME1 expression.

ME1 absence sensitizes cells to ferroptotic cell death with erastin

Elevated levels of ROS and increases in the labile iron pool are both associated with susceptibility to cell death by ferroptosis (37, 68). Therefore, it was hypothesized that ME1-null cells would exhibit increased sensitivity to erastin, an established inducer of ferroptosis (69, 70). Cell death with erastin treatment was compared in ME1-expressing cells (SYO OE, Fuji OE, and HTB93 WT) and ME1-null or -deficient cells (SYO WT, Fuji WT, and HTB-93 KD2 and KD3). Treatment with erastin resulted in significantly increased cell death in cells that do not express ME1 (SYO-1 WT and Fuji WT) compared with ME1-overexpressing cells (SYO-1 OE and Fuji OE; **Fig. 5A** and **B**). However, partial KD of ME1 in HTB-93 was likely not sufficient to induce significantly higher levels of cell death with erastin relative to HTB-93 WT cell lines (Supplementary Fig. S12a). Treatment of vector control cell lines with erastin confirmed that changes in sensitivity to erastin treatment were dependent upon ME1 expression and were unrelated to the vector (Supplementary Fig. S13a and S13b).

Ferroptosis is often associated with high levels of lipid peroxidation; therefore, the lipid peroxidation-mediated cell death in response to erastin was investigated in WT ME1-null SS (71–73). Cell death with erastin in combination with lipophilic antioxidants (Trolox and alpha-tocopherol) and ferrostatin was compared with treatment with erastin alone. Cotreatment with lipophilic antioxidants as well as ferrostatin significantly attenuated cell death in both SYO-1 WT ME1-null and Fuji WT ME1-null cells (**Fig. 5C** and **D**). Furthermore, lipid peroxidation with and without erastin treatment was measured using the Image-IT live-cell imaging probe. As expected, erastin treatment induced significantly more lipid peroxidation in cells that do not express ME1 when compared with ME1-expressing cells (**Fig. 5E** and **F**). Similarly, erastin treatment resulted in significantly more lipid peroxidation in HTB-93 ME1 KD cells relative to HTB-93 WT cells (Supplementary Fig. S12b). Cumulatively these data indicate that erastin induces cell death via a lipid peroxidation-dependent mechanism, and the attenuation of cell death in response to ferrostatin suggests that cell death occurs through ferroptosis.

Accumulation of iron is a common feature of cancer metabolism, which can not only fuel ROS production leading to ferroptosis, but also contributes to cellular growth and cell survival (39). Therefore, cellular dependence on elevated labile iron pools in the context of ME1 absence was evaluated. Deferasirox, a nonredox active iron chelator, was used to chelate the free iron, and cellular response in SS WT ME1-null and ME1 OE cell lines was compared. Death was significantly induced in both SYO-1 and Fuji WT ME1-null lines, whereas minimal cell death was induced in the ME1-OE cell lines (**Fig. 5G**). Additionally, when ME1 was knocked down in HTB-93, these cells became sensitive to deferasirox treatment (**Fig. 5H**; Supplementary Fig. S14a). Treatment of vector control cell lines with deferasirox confirmed that changes in sensitivity to deferasirox treatment were dependent upon ME1 expression and were unrelated to the vector (Supplementary Fig. S14b and S14c). These data establish that ME1-null cells are dependent upon labile iron pools. This dependency suggests that escape from ferroptosis induction is not likely achievable through reductions to labile iron pool in this context. Collectively these data support the exploration of ferroptosis induction as a viable translational target for ME1-null SS.

Exploiting alterations in ROS homeostasis and the glutathione/thioredoxin axis at cystine import

The proposed mechanism of erastin is inhibition of cystine import through xCT, leading to lipid peroxidation and ferroptosis (**Fig. 6A**; ref. 37). Cystine imported by xCT is rapidly converted to cysteine in the intracellular environment. Within this study, it has been demonstrated

(*Continued.*) **C,** Average normalized isotopomer abundance from stable isotope tracing of $U^{13}C$-glutamine in reduced glutathione (GSH; top) and oxidized glutathione (GSSG; bottom) over time in ME1-null SS cell line Fuji WT and ME1-overexpressing cell line Fuji OE. Isotopomer abundance was normalized to cell count. **D,** *In vitro* cell death response to BSO inhibition of gamma-glutamyl I in ME1-null SS cell lines (SYO-1 WT and Fuji WT), ME1 overexpression cell lines (SYO-1 OE and Fuji OE), ME1-expressing cell lines (HTB-93 WT), and ME1 KD cell lines (HTB-93 KD1). Data, mean ± SD ($n = 3$); ****, $P < 0.0001$; ***, $P < 0.001$; **, $P < 0.01$. **E,** Relative fluorescence measurements (RFU) of global thiol levels to treatment with BSO relative to no treatment (NT) in ME1-null SS cell line SYO-1 WT and ME1-overexpressing cell line SYO-1 OE. Data, mean ± SD ($n = 3$); **, $P < 0.01$; ****, $P < 0.0001$. **F,** Relative fluorescence measurements (RFU) of global thiol levels to treatment with BSO relative to NT in ME1-null SS cell line Fuji WT and ME1-overexpressing cell line Fuji OE. Data, mean ± SD ($n = 3$); ***, $P < 0.001$; ****, $P < 0.0001$. **G,** *In vitro* cell death response to D9 inhibition of thioredoxin reductase in ME1-null SS cell lines (SYO-1 WT, Fuji WT), ME1 overexpression cell lines (SYO-1 OE and Fuji OE), ME1-expressing cell line (HTB-93 WT), and ME1 KD cell line (HTB-93 KD1). Data, mean ± SD ($n = 3$); ****, $P < 0.0001$; **, $P < 0.01$. **H,** Relative fold change of H_2O_2 in ME1-null SS cell lines (SYO-1 WT and Fuji WT) and ME1 overexpression cell lines (SYO-1 OE and Fuji OE). Data, mean ± SD ($n = 3$); **, $P < 0.01$. **I,** Relative fold change of $Fe2^+$ levels in ME1-null SS cell lines (SYO-1 WT and Fuji WT) and ME1 overexpression cell lines (SYO-1 OE and Fuji OE) at baseline. Data, mean ± SD ($n = 3$); **, $P < 0.01$; ***, $P < 0.001$.

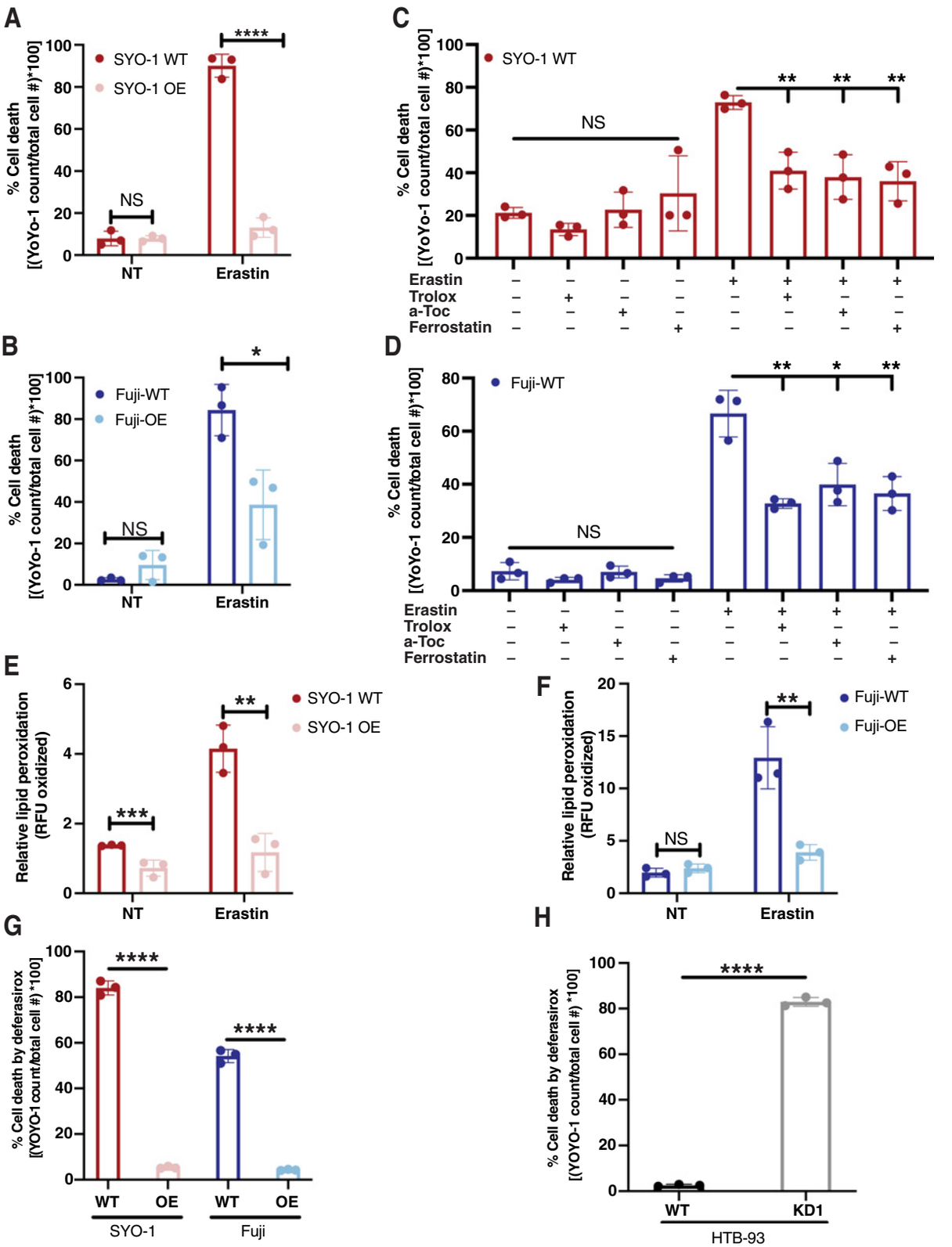
A
% Cell death [(YoYo-1 count/total cell #)*100]
SYO-1 WT
SYO-1 OE
****
NS
NT
Erastin
B
% Cell death [(YoYo-1 count/total cell #)*100]
Fuji-WT
Fuji-OE
*
NS
NT
Erastin
C
% Cell death [(YoYo-1 count/total cell #)*100]
SYO-1 WT
**
**
**
NS
Erastin
Trolox
a-Toc
Ferrostatin
D
% Cell death [(YoYo-1 count/total cell #)*100]
Fuji-WT
**
*
**
NS
Erastin
Trolox
a-Toc
Ferrostatin
E
Relative lipid peroxidation (RFU oxidized)
SYO-1 WT
SYO-1 OE
**
***
NT
Erastin
F
Relative lipid peroxidation (RFU oxidized)
Fuji-WT
Fuji-OE
**
NS
NT
Erastin
G
% Cell death by deferasirox [(YOYO-1 count/total cell #) *100]
****
****
WT
OE
WT
OE
SYO-1
Fuji
H
% Cell death by deferasirox [(YOYO-1 count/total cell #) *100]
****
WT
KD1
HTB-93

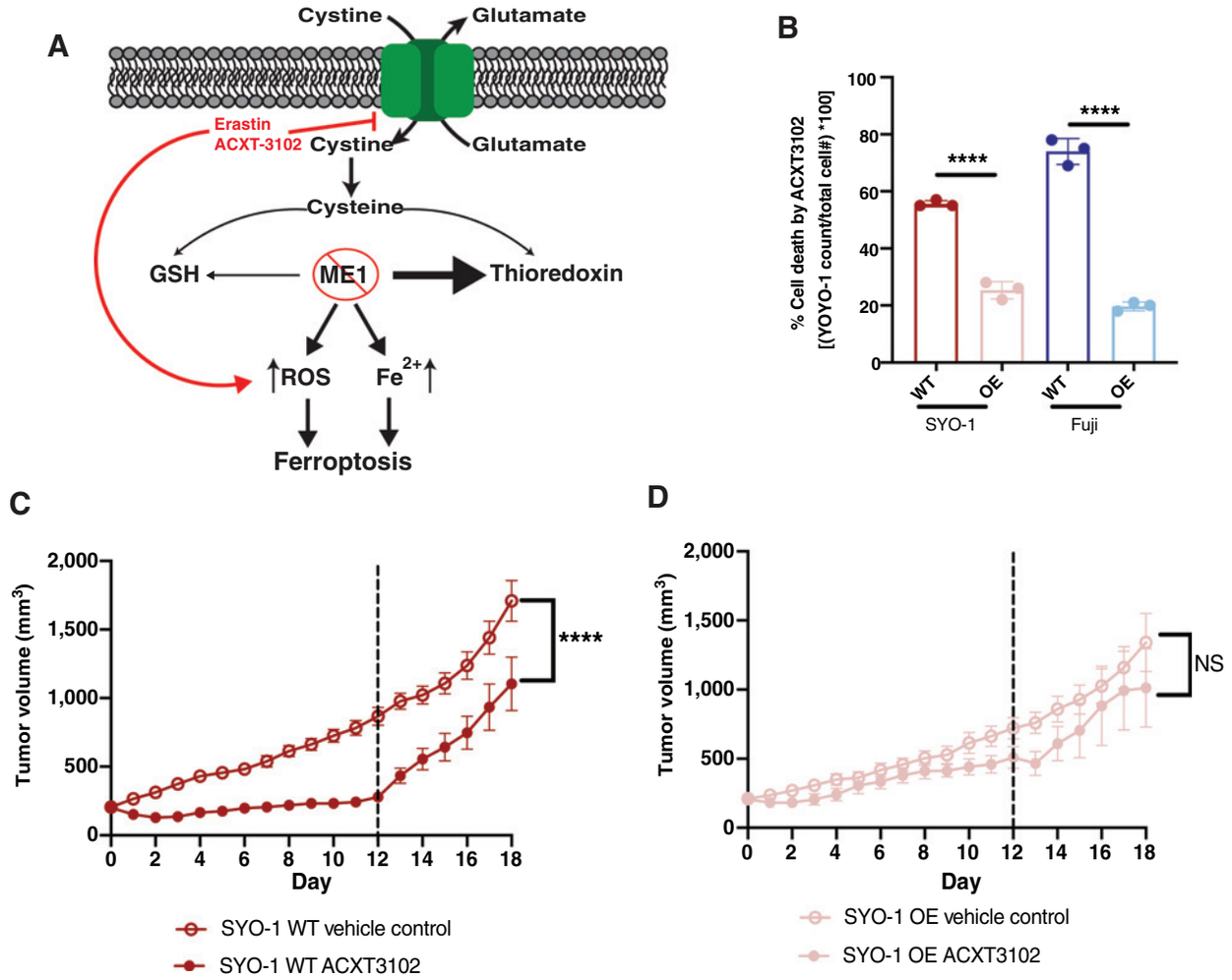

Figure 6.
Exploiting alterations in ROS homeostasis and the glutathione/thioredoxin axis at cystine import. **A,** Schematic diagram: xCT: glutamine-cystine antiporter (SLC3A2 and SLC7A11); ME1: malic enzyme 1; GSH: representing glutathione antioxidant system; thioredoxin: representing thioredoxin antioxidant system. **B,** *In vitro* cell death in response to ACXT-3102 (Sigma-2/erastin) inhibition of xCT in ME1-null SS cell lines (SYO-1 WT and Fuji WT) and ME1-overexpressing cell lines (SYO-1 OE and Fuji OE). Data, mean ± SD ($n = 3$); ****, $P < 0.0001$. **C,** Tumor volume of SYO-1 WT ME1-null xenografts treated until day 12 with ACXT-3102 ($n = 10$) (ACXT-3102) or vehicle ($n = 10$). Data, mean ± SEM; ****, $P < 0.0001$. **D,** Tumor volume of SYO-1 ME1-OE xenografts treated until day 12 with ACXT-3102 ($n = 10$) (ACXT-3102) or vehicle ($n = 10$). Data, mean ± SEM; NS, $P > 0.05$.

that ME1-deficient cells exhibit changes to systems that depend on intracellular cysteine, the thioredoxin and glutathione systems. Therefore, cysteine metabolism may also contribute to increased erastin sensitivity in cells that lack expression of ME1. Cystine uptake was measured using an FITC-cystine probe in SS WT ME1-null and ME1 OE cell lines, revealing that ME1 expression does not alter cystine uptake rates in SS (Supplementary Fig. S15a and S15b). However, measurements of intracellular cysteine via mass spectrometry revealed

Figure 5.
ME1 absence sensitizes cells to ferroptotic cell death with erastin. **A,** *In vitro* cell death in response to erastin (1 μmol/L) in ME1-null SS cell line SYO-1 WT and ME1 overexpression cell line SYO-1 OE. Data, mean ± SD ($n = 3$); ****, $P < 0.0001$; NS, $P > 0.05$. **B,** *In vitro* cell death in response to erastin (2 μmol/L) in the ME1-null SS cell line Fuji WT and ME1 overexpression cell line Fuji OE. Data, mean ± SD ($n = 3$); *, $P < 0.05$; NS, $P > 0.05$. **C,** *In vitro* cell death in response to erastin (1 μmol/L) ± Trolox, a-tocopherol (a-Toc), or ferrostatin in ME1-null SS cell line SYO-1. Data, mean ± SD ($n = 3$); **, $P < 0.01$; NS, $P > 0.05$. **D,** *In vitro* cell death in response to erastin (2 μmol/L) ± Trolox, a-tocopherol (a-Toc), or ferrostatin in ME1-null SS cell line Fuji WT. Data, mean ± SD ($n = 3$); **, $P < 0.01$; *, $P < 0.05$; NS, $P > 0.05$. **E,** Relative fluorescence measurements (RFU) of lipid peroxidation to treatment with erastin (1 μmol/L) relative to NT in ME1-null SS cell line SYO-1 WT and ME1-overexpressing cell line SYO-1 OE. Data, mean ± SD ($n = 3$); ***, $P < 0.001$; **, $P < 0.01$. **F,** Relative fluorescence measurements (RFU) of lipid peroxidation to treatment with erastin (4 μmol/L) relative to NT in ME1-null SS cell line Fuji WT and ME1-overexpressing cell line Fuji OE. Data, mean ± SD ($n = 3$); **, $P < 0.01$; NS, $P > 0.05$. **G,** *In vitro* cell death in response to deferasirox iron chelation in ME1-null SS cell lines (SYO-1 WT and Fuji WT) and ME1 overexpression cell lines (SYO-1 OE and Fuji OE). Data, mean ± SD ($n = 3$); ****, $P < 0.0001$. **H,** *In vitro* cell death in response to deferasirox iron chelation in ME1-expressing cell lines (HTB-93 WT) and ME1-KD cell lines (HTB-93 KD1). Data are represented as mean ± SD ($n = 3$); ****, $P < 0.0001$.

that ME1-null cells exhibit significantly reduced intracellular cysteine pools compared with ME1-expressing SS (Supplementary Fig. S15c). These data suggest that elevated demand for intracellular cysteine to fuel cellular antioxidant systems may also contribute to increased erastin sensitivity in WT ME1-null compared with ME1 OE SS cells.

Erastin, although a potent inhibitor of xCT *in vitro*, has failed to translate clinically in human trials, likely due to poor tumor targeting and uptake (74, 75). Therefore, to evaluate the effect of xCT inhibition with a clinically relevant compound *in vivo*, the efficacy of an erastin conjugate molecule, ACXT-3102 in WT ME1-null and ME1 OE SS cell lines was tested. ACXT-3102 is a sigma-2 ligand-conjugated erastin compound with increased intracellular import, which similarly inhibits xCT (76, 77). As expected, treatment with ACXT-3102 recapitulated the cell death response induced by erastin, demonstrating higher levels of cell death in WT ME1-null SS cells relative to ME1 OE SS cells (**Fig. 6B**).

Furthermore, to evaluate the *in vivo* efficacy of ACXT-3102 treatment in SYO-1 WT ME1-null and ME1 OE *in vivo*. Xenografts were grown to 200 mm^3 prior to treatment initiation with oral ACXT-3102 for 12 days at 60 mg/kg. The effect on tumor growth was measured daily (**Fig. 6C** and **D**). Relative to vehicle-treated xenografts ($n = 10$), the growth of SYO-1 WT ME1-null tumors treated with ACXT-3102 ($n = 10$) was inhibited (**Fig. 6C**). However, treatment with ACXT-3102 failed to inhibit tumor growth in SYO-1 OE tumors ($n = 10$), resulting in no significant difference between the vehicle-treated xenografts ($n = 10$) and the ACXT-3102-treated xenografts at the dose utilized (**Fig. 6D**). These data suggest that not only is disruption of redox homeostasis using xCT inhibition a valid translational target in SS, but that the response to xCT inhibition in this context is dependent upon the ME1 expression status of the tumor.

Discussion

SS arises from a characteristic chromosomal translocation between *SS18* and *SSX* that drives broad changes in chromatin remodeling and gene transcription (78). As there is a clinical need for the development of highly effective, targeted therapeutics for SS, we hypothesized that understanding SS metabolism would reveal a therapeutic opportunity. Within this study, metabolic characterization identified SS as the first cancer that recurrently lacks expression of ME1. Although cancers have been associated with an overexpression in ME1, this is the first-in-class example of a cancer that consistently lacks expression of ME1. Cancer metabolism is often inherited from the cell of origin (79, 80). Consistent with this body of literature, we demonstrated that the absence of ME1 expression in SS appears to be linked to the absence of ME1 in the recently proposed cell of origin; however, determination of the cell of origin for SS is an active field an additional research may be necessary to corroborate this finding in future studies (81). Without ME1 expression, SS exhibits increased reliance on the thioredoxin pathway and alterations in iron redox biology. Therefore, these findings provide a rationale for the utilization of therapies to exploit the innate redox biology in ME1-null cancers.

Metabolomic analysis of ME1-null SS cell lines revealed that glucose catabolism occurred primarily through glycolysis, and that glucose was preferentially directed through the oxPPP. Increased flux of glucose through the oxPPP contributes to the production of NADPH in the absence of ME1. Disrupting the ability of SS to produce NADPH through the oxPPP by inhibiting G6PD with G6PDi-1 resulted in cell death *in vitro*. This correlates with previous findings that knockdown of ME1 in ME1-overexpressing cancers altered cellular NADPH production and increased dependency upon the oxPPP (18, 59).

ME1 knockdown results in a depletion of total cellular GSH, suggesting altered redox biology related to the glutathione pathway. We have found that ME1-null SS exhibits an underactive glutathione pathway, whereas dependence upon thioredoxin pathway activity is significantly increased in the context of ME1 absence. Preferential utilization of the thioredoxin pathway over the glutathione pathway for the maintenance of redox homeostasis has been described in the literature, but the underlying mechanisms are poorly understood (82, 83). More studies are needed to fully understand the role of the thioredoxin system in ME1-deficient cancers. However, this work contributes to the growing body of evidence that emphasizes the importance of the thioredoxin system as a potential therapeutic target in cancer (84–86).

ME1 knockdowns have demonstrated increased sensitivity to redox stress (18). Similarly, we have identified key metabolic alterations that increase baseline ROS and susceptibility to the induction of redox stress in ME1-null SS. ME1-null SS exhibits increased H_2O_2 and labile iron pools, which promote Fenton reaction activity and ROS accumulation. Consistent with the demonstrated increase in ROS and liable iron pools, ME1-null SS exhibits increased sensitivity to erastin-induced lipid peroxidation and ferroptosis. Critically, the enhanced dependency upon an elevated labile iron pool coupled with reduced glutathione pathway capacity uniquely primes ME1-null SS for ferroptosis induction and supports the development of treatment strategies targeting the ferroptotic pathway in SS.

Erastin has underperformed in clinical trials, and this lack of efficacy is due to the inability of the drug to be efficiently taken up by cancer cells (76). This uptake blockade can be overcome by conjugating erastin to a sigma-2 ligand to enhance xCT receptor interaction. This conjugation forms a more efficacious construct, Sigma-2/erastin (ACXT-3102; refs. 76, 77, 87–92). Inhibition of xCT with ACXT-3102 induced rapid death in WT ME1-null SS cells, and cell death was protected by ME1 expression. Furthermore, in SYO-1 WT ME1-null xenografts, ACXT-3102 treatment significantly impaired tumor growth. Importantly, SYO-1 ME1 OE xenograft mice did not exhibit significant tumor response to treatment with ACXT-3102 at the dosage used. These data indicate that ME1 absence is a predictive biomarker for sensitivity to xCT inhibition and further support the development of treatment strategies targeting the ferroptotic pathway in SS.

This study is the first to characterize the metabolism of synovial sarcoma. Within this study, novel metabolic vulnerabilities have been uncovered in SS. Importantly, the recurrent absence of ME1 has been identified in SS. Although studies have demonstrated that ME1 is frequently overexpressed in cancer, this is the first study to identify a cancer where ME1 is not expressed recurrently and predictably. ME1 is thought to play an essential role in maintaining redox homeostasis within the cell. With insufficient expression of ME1, ME1-null SS adapts to maintain the redox homeostasis; however, these adaptations can be easily disrupted. By exploiting alterations in redox homeostasis with ACXT-3102 inhibition of xCT, a new treatment strategy for ME1-null cancers can be developed. Additionally, inhibition of xCT could provide a targeted treatment for a broader group of patients with cancers overexpressing ME1; however, these findings await the identification of a selective ME1 inhibitor, which is currently under development.

Authors' Disclosures

B.C. Prudner reports other support from Miltenyi Biomedicine outside the submitted work. R. Rathore reports personal fees from Natera outside the submitted work. D. Spitzer reports grants from NIH (R01 CA163764) and personal fees from

Accuronix Therapeutics during the conduct of the study as well as personal fees from Accuronix Therapeutics outside the submitted work; in addition, D. Spitzer has patent US10087175B2 issued and licensed to Accuronix Therapeutics. T.O. Nielsen reports grants from Canadian Cancer Society (grant 705615) during the conduct of the study as well as other support from Bioclassifier LLC outside the submitted work; in addition, T.O. Nielsen has a patent for PAM50/Prosigna issued, licensed, and with royalties paid from Veracyte. E.B. Taylor reports grants from NIH during the conduct of the study. W. Hawkins reports grants from NCI (NCI-P50CA196510 and NCI-R01CA163764) and other support from Accuronix during the conduct of the study as well as grants from Celldex outside the submitted work; in addition, W.G. Hawkins has a patent for ACXT-3102 composition of matter issued and licensed to Accuronix. B.A. Van Tine reports grants, personal fees, and other support from Accuronix Therapeutics and grants and other support from patent 11175296 during the conduct of the study as well as grants from Pfizer, Merck, and Tracon Pharm; grants, personal fees, and other support from GSK; personal fees from Epizyme, ADRx, Ayala Pharmaceuticals, Cytokinetics Inc, Bayer, Adaptimmune Limited, Apexigen Inc, Daiichi Sankyo, Deciphera Pharmaceuticals, Inc, Novartis, and Lilly; and other support from Polaris, Targeted Oncology, Bionest Partners, and Intellisphere LLC outside the submitted work; in addition, B.A. Van Tine has a patent 11175296 issued and a patent on ACXT3102 issued. No disclosures were reported by the other authors.

Authors' Contributions

C.B. Brashears: Formal analysis, investigation, methodology, writing–original draft, writing–review and editing. **B.C. Prudner:** Data curation, formal analysis, investigation, writing–original draft, writing–review and editing. **R. Rathore:** Data curation, investigation, writing–review and editing. **K.E. Caldwell:** Data curation, investigation, writing–review and editing. **C.A. Dehner:** Data curation, writing–review and editing. **J.L. Buchanan:** Data curation, methodology, writing–review and editing. **S.E.S. Lange:** Data curation, formal analysis, investigation, writing–review and editing. **N. Poulin:** Data curation, writing–review and editing. **J.K. Sehn:** Data curation, writing–review and editing. **J. Roszik:** Data curation, writing–review and editing. **D. Spitzer:** Data curation, supervision, writing–review and editing. **K.B. Jones:** Data curation, writing–review and editing. **R. O'Keefe:** Data curation, writing–review and editing. **T.O. Nielsen:** Resources, data curation, writing–review and editing. **E.B. Taylor:** Resources, writing–review and editing. **J.M. Held:** Formal analysis, writing–review and editing. **W. Hawkins:** Resources, writing–review and editing. **B.A. Van Tine:** Conceptualization, data curation, formal analysis, supervision, funding acquisition, validation, investigation, visualization, methodology, writing–original draft, project administration, writing–review and editing.

Acknowledgments

The authors would like to thank the following funding sources: NCI R01 CA227115 (B.A. Van Tine), CJ's Journey (B.A. Van Tine and R. Rathore), Wipe Out Kids Cancer (B.A. Van Tine and S.E.S. Lange), The Sarcoma Foundation of America (B.A. Van Tine and B.C. Prudner), the Sarcoma Alliance for Research and Collaboration (B.A. Van Tine and C.B. Brashears), the Canadian Cancer Society Grant #701582 (T.O. Nielsen), the Sarcoma Cancer Foundation of Canada Beth England's Sarcoma Research Fund (T.O. Nielsen), the Pedal for Home Impact Grant of the Canadian Cancer Society grant #705615 (T.O. Nielsen), Washington University in St. Louis School of Medicine MSTP training grant #5T32GM007200 (C.B. Brashears), NCI R01 CA163764 (W. Hawkins and D. Spitzer), Washington University Surgical Oncology Training Grant #T32CA009621 (K.E. Caldwell), NIH R01 DK104998 (E.B. Taylor), NIDDK F30 DK127845 (J.L. Buchanan), and University of Iowa Medical Scientist Training Program #T32TGM007337 (J.L. Buchanan) to Steven Lentz and Pamela Geyer. The results represented here are in whole or part based upon data generated by the TCGA Research Network: https://www.cancer.gov/tcga. We would like to thank the lab of Dr. Rabinowitz for their generous gift of G6PDi-1.

The publication costs of this article were defrayed in part by the payment of publication fees. Therefore, and solely to indicate this fact, this article is hereby marked "advertisement" in accordance with 18 USC section 1734.

Note

Supplementary data for this article are available at Clinical Cancer Research Online (http://clincancerres.aacrjournals.org/).

Received February 14, 2022; revised March 29, 2022; accepted April 12, 2022; published first April 14, 2022.

References

1. Barrott JJ, Illum BE, Jin H, Hedberg ML, Wang Y, Grossmann A, et al. Paracrine osteoprotegerin and β-catenin stabilization support synovial sarcomagenesis in periosteal cells. J Clin Invest 2018;128:207–18.
2. Clark J, Rocques PJ, Crew AJ, Gilp S, Shipley J, Chan AM, et al. Identification of novel genes, SYT and SSX, involved in the t(X;18)(p11.2;q11.2) translocation found in human synovial sarcoma. Nat Genet 1994;7:502–8.
3. De Bruijn DRH, Allander SV, Van Dijk AHA, Willemse MP, Thijssen J, Van Groningen JJM, et al. The synovial sarcoma-associated SS18-SSX2 fusion protein induces epigenetic gene (de)regulation. Cancer Res 2006;66:9474–82.
4. Kadoch C, Crabtree GR. Reversible disruption of mSWI/SNF (BAF) complexes by the SS18-SSX oncogenic fusion in synovial sarcoma. Cell 2013;153:71–85.
5. Sandberg AA. Updates on the cytogenetics and molecular genetics of bone and soft tissue tumors: liposarcoma. Cancer Genet Cytogenet 2004;155:1–24.
6. Ferrari A, Gronchi A, Casanova M, Meazza C, Gandola L, Collini P, et al. Synovial sarcoma: a retrospective analysis of 271 patients of all ages treated at a single institution. Cancer 2004;101:627–34.
7. Singer S, Baldini EH, Demetri GD, Fletcher JA, Corson JM. Synovial sarcoma: prognostic significance of tumor size, margin of resection, and mitotic activity for survival. J Clin Oncol 1996;14:1201–8.
8. Stacchiotti S, Van Tine BA. Synovial sarcoma: current concepts and future perspectives. J Clin Oncol 2018;36:180–7.
9. Zhu Y, Gu L, Lin X, Liu C, Lu B, Cui K, et al. Dynamic regulation of ME1 phosphorylation and acetylation affects lipid metabolism and colorectal tumorigenesis. Mol Cell 2020;77:138–49.
10. Shi Y, Zhou S, Wang P, Guo Y, Xie B, Ding S. Malic enzyme 1 (ME1) is a potential oncogene in gastric cancer cells and is associated with poor survival of gastric cancer patients. Onco Targets Ther 2019;12:5589–99.
11. Liu M, Chen Y, Huang B, Mao S, Cai K, Wang L, et al. Tumor-suppressing effects of microRNA-612 in bladder cancer cells by targeting malic enzyme 1 expression. Int J Oncol 2018;52:1923–33.
12. Lu YX, Ju HQ, Liu ZX, Chen DL, Wang Y, Zhao Q, et al. ME1 regulates NADPH homeostasis to promote gastric cancer growth and metastasis. Cancer Res 2018;78:1972–85.
13. Nakashima C, Yamamoto K, Fujiwara-Tani R, Luo Y, Matsushima S, Fujii K, et al. Expression of cytosolic malic enzyme (ME1) is associated with disease progression in human oral squamous cell carcinoma. Cancer Sci 2018;109:2036–45.
14. Chakrabarti G. Mutant KRAS associated malic enzyme 1 expression is a predictive marker for radiation therapy response in non-small cell lung cancer. Radiat Oncol 2015;10:145–52.
15. Liao R, Ren G, Liu H, Chen X, Cao Q, Wu X. ME1 promotes basal-like breast cancer progression and associates with poor prognosis. Sci Rep 2018;8:16743.
16. Wen D, Liu D, Tang J, Dong L, Liu Y, Tao Z, et al. Malic enzyme 1 induces epithelial–mesenchymal transition and indicates poor prognosis in hepatocellular carcinoma. Tumor Biol 2015;36:6211–21.
17. Son J, Lyssiotis CA, Ying H, Wang X, Hua S, Ligorio M, et al. Glutamine supports pancreatic cancer growth through a KRAS-regulated metabolic pathway. Nature 2013;496:101–5.
18. Wang QQ, Zhang ZY, Xiao JY, Yi C, Li LZ, Huang Y, et al. Repressing malic enzyme 1 redirects glucose metabolism unbalances the redox state, and attenuates migratory and invasive abilities in nasopharyngeal carcinoma cell lines. Chin J Cancer 2012;31:588–97.
19. Hsu RY. Pigeon liver malic enzyme. Mol Cell Biochem 1982;43:3–26.
20. Frenkel R. Regulation and physiological functions of malic enzymes. Curr Top Cell Regul 1975;9:157–81.
21. Edens WA, Urbauer JL, Cleland WW. Determination of the chemical mechanism of malic enzyme by isotope effects. Biochemistry 1997;36:1141–7.
22. Fan J, Ye J, Kamphorst JJ, Shlomi T, Thompson CB, Rabinowitz JD. Quantitative flux analysis reveals folate-dependent NADPH production. Nature 2014;510:298–302.

23. Lin R, Elf S, Shan C, Kang HB, Ji Q, Zhou L, et al. 6-Phosphogluconate dehydrogenase links oxidative PPP, lipogenesis and tumour growth by inhibiting LKB1-AMPK signalling. Nat Cell Biol 2015;17:1484–96.
24. Dang L, Yen K, Attar EC. IDH mutations in cancer and progress toward development of targeted therapeutics. Ann Oncol 2016;27:599–608.
25. Jiang P, Du W, Mancuso A, Wellen KE, Yang X. Reciprocal regulation of p53 and malic enzymes modulates metabolism and senescence. Nature 2013;493: 689–93.
26. DeBerardinis RJ, Mancuso A, Daikhin E, Nissim I, Yudkoff M, Wehrli S, et al. Beyond aerobic glycolysis: transformed cells can engage in glutamine metabolism that exceeds the requirement for protein and nucleotide synthesis. Proc Natl Acad Sci 2007;104:19345–50.
27. CHANG G-G, WANG J-K, HUANG T-M, LEE H-J, CHOU W-Y, MENG C-L. Purification and characterization of the cytosolic NADP+-dependent malic enzyme from human breast cancer cell line. Eur J Biochem 1991;202:681–8.
28. Sena LA, Chandel NS. Physiological roles of mitochondrial reactive oxygen species. Mol Cell 2012;48:158–67.
29. Wiseman H, Halliwell B. Damage to DNA by reactive oxygen and nitrogen species: role in inflammatory disease and progression to cancer. Biochem J 1996; 313:17–29.
30. Trachootham D, Zhou Y, Zhang H, Demizu Y, Chen Z, Pelicano H, et al. Selective killing of oncogenically transformed cells through a ROS-mediated mechanism by β-phenylethyl isothiocyanate. Cancer Cell 2006;10:241–52.
31. Lee S, Kim SM, Lee RT. Thioredoxin and thioredoxin target proteins: from molecular mechanisms to functional significance. Antioxid Redox Signal 2013; 18:1165–207.
32. Meister A, Anderson ME. Glutathione. Annu Rev Biochem 1983;52:711–60.
33. Amstad P, Moret R, Cerutti P. Glutathione peroxidase compensates for the hypersensitivity of Cu,Zn- superoxide dismutase overproducers to oxidant stress. J Biol Chem 1994; 269:1606–9.
34. Teixeira HD, Meneghini R. Chinese hamster fibroblasts overexpressing CuZn-superoxide dismutase undergo a global reduction in antioxidants and an increasing sensitivity of DNA to oxidative damage. Biochem J 1996;315: 821–5.
35. Seefeldt T, Zhao Y, Chen W, Raza AS, Carlson L, Herman J, et al. Characterization of a novel dithiocarbamate glutathione reductase inhibitor and its use as a tool to modulate intracellular glutathione. J Biol Chem 2009;284: 2729–37.
36. Kranich O, Dringen R, Sandberg M, Hamprecht B. Utilization of cysteine and cysteine precursors for the synthesis of glutathione in astroglial cultures: preference for cystine. Glia. United States; 1998;22:11–8.
37. Dixon SJ, Lemberg KM, Lamprecht MR, Skouta R, Zaitsev EM, Gleason CE, et al. Ferroptosis: an iron-dependent form of nonapoptotic cell death. Cell 2012;149: 1060–72.
38. Dixon SJ, Stockwell BR. The hallmarks of ferroptosis. Annu Rev Cancer Biol 2019;3:35–54.
39. Torti SV, Torti FM. Iron and cancer: more ore to be mined. Nat Rev Cancer 2013; 13:342–55.
40. Kawano S, Grassian AR, Tsuda M, Knutson SK, Warholic NM, Kuznetsov G, et al. Preclinical evidence of anti-tumor activity induced by EZH2 inhibition in human models of synovial sarcoma. PLoS One 2016;11:1–22.
41. Nakayama R, Mitani S, Nakagawa T, Hasegawa T, Kawai A, Morioka H, et al. Gene expression profiling of synovial sarcoma: distinct signature of poorly differentiated type. Am J Surg Pathol 2010;34:1599–607.
42. Chibon F, Lagarde P, Salas S, Pérot G, Brouste V, Tirode F, et al. Validated prediction of clinical outcome in sarcomas and multiple types of cancer on the basis of a gene expression signature related to genome complexity. Nat Med 2010;16:781–7.
43. Gibault L, Ferreira C, Pérot G, Audebourg A, Chibon F, Bonnin S, et al. From PTEN loss of expression to RICTOR role in smooth muscle differentiation: complex involvement of the mTOR pathway in leiomyosarcomas and pleomorphic sarcomas. Mod Pathol 2012;25:197–211.
44. Doyle KR, Mitchell MA, Roberts CL, James S, Johnson JE, Zhou Y, et al. Validating a gene expression signature proposed to differentiate liposarcomas that use different telomere maintenance mechanisms. Oncogene 2012; 31:265–6.
45. Sears DD, Hsiao G, Hsiao A, Yu JG, Courtney CH, Ofrecio JM, et al. Mechanisms of human insulin resistance and thiazolidinedione-mediated insulin sensitization. Proc Natl Acad Sci U S A 2009;106:18745–50.
46. Hardy OT, Perugini RA, Nicoloro SM, Gallagher-Dorval K, Puri V, Straubhaar J, et al. Body mass index-independent inflammation in omental adipose tissue associated with insulin resistance in morbid obesity. Surg Obes Relat Dis 2011;7: 60–7.
47. Plaisier CL, Kyttälä M, Weissglas-Volkov D, Sinsheimer JS, Huertas-Vazquez A, Riba L, et al. Galanin preproprotein is associated with elevated plasma triglycerides. Arterioscler Thromb Vasc Biol 2009;29:147–52.
48. Johansson LE, Danielsson APH, Parikh H, Klintenberg M, Norstrom̈ F, Groop L, et al. Differential gene expression in adipose tissue from obese human subjects during weight loss and weight maintenance. Am J Clin Nutr 2012;96:196–207.
49. Skov V, Glintborg D, Knudsen S, Jensen T, Kruse TA, Tan Q, et al. Reduced expression of nuclear-encoded genes involved in mitochondrial oxidative metabolism in skeletal muscle of insulin-resistant women with polycystic ovary syndrome. Diabetes 2007;56:2349–55.
50. Keller P, Vollaard NBJ, Gustafsson T, Gallagher IJ, Sundberg CJ, Rankinen T, et al. A transcriptional map of the impact of endurance exercise training on skeletal muscle phenotype. J Appl Physiol 2011;110:46–59.
51. Gentleman RC, Carey VJ, Bates DM, Bolstad B, Dettling M, Dudoit S, et al. Bioconductor: open software development for computational biology and bioinformatics. Genome Biol 2004;5:R80.
52. Wilson CL, Miller CJ. Simpleaffy: a bioconductor package for affymetrix quality control and data analysis. Bioinformatics 2005;21:3683–5.
53. Freue GVC, Hollander Z, Shen E, Zamar RH, Balshaw R, Scherer A, et al. MDQC: a new quality assessment method for microarrays based on quality control reports. Bioinformatics 2007;23:3162–9.
54. Wu Z, Irizarry RA, Gentleman R, Martinez-Murillo F, Spencer F. A model-based background adjustment for oligonucleotide expression arrays. J Am Stat Assoc 2004;99:909–17.
55. Zhang YJ, Wang Z, Sprous D, Nabioullin R. In silico design and synthesis of piperazine-1-pyrrolidine-2,5-dione scaffold-based novel malic enzyme inhibitors. Bioorganic Med Chem Lett 2006;16:525–8.
56. Jones KB, Barrott JJ, Xie M, Haldar M, Jin H, Zhu JF, et al. The impact of chromosomal translocation locus and fusion oncogene coding sequence in synovial sarcomagenesis. Oncogene 2016;35:5021–32.
57. Haldar M, Hancock JD, Coffin CM, Lessnick SL, Capecchi MR. A conditional mouse model of synovial sarcoma: insights into a myogenic origin. Cancer Cell 2007;11:375–88.
58. Abeshouse A, Adebamowo C, Adebamowo SN, Akbani R, Akeredolu T, Ally A, et al. Comprehensive and integrated genomic characterization of adult soft tissue sarcomas. Cell 2017;171:950–65.
59. Murai S, Ando A, Ebara S, Hirayama M, Satomi Y, Hara T. Inhibition of malic enzyme 1 disrupts cellular metabolism and leads to vulnerability in cancer cells in glucose-restricted conditions. Oncogenesis 2017;6:1–9.
60. Mookerjee SA, Goncalves RLS, Gerencser AA, Nicholls DG, Brand MD. The contributions of respiration and glycolysis to extracellular acid production. Biochim Biophys Acta - Bioenerg 2015;1847:171–81.
61. Divakaruni AS, Paradyse A, Ferrick DA, Murphy AN, Jastroch M. Analysis and interpretation of microplate-based oxygen consumption and pH data. 1st ed. Methods Enzymol 2014;547:309–54.
62. Lee WNP, Boros LG, Puigjaner J, Bassilian S, Lim S, Cascante M. Mass isotopomer study of the nonoxidative pathways of the pentose cycle with [1,2-13C2]glucose. Am J Physiol - Endocrinol Metab 1998;274: 843–51.
63. Chen L, Zhang Z, Hoshino A, Zheng HD, Morley M, Arany Z, et al. NADPH production by the oxidative pentose-phosphate pathway supports folate metabolism. Nat Metab 2019;1:404–15.
64. Ghergurovich JM, García-Cañaveras JC, Wang J, Schmidt E, Zhang Z, TeSlaa T, et al. A small molecule G6PD inhibitor reveals immune dependence on pentose phosphate pathway. Nat Chem Biol 2020;16:731–9.
65. Zhang D, Xu Z, Yuan J, Zhao YX, Qiao ZY, Gao YJ, et al. Synthesis and molecular recognition studies on small-molecule inhibitors for thioredoxin reductase. J Med Chem 2014;57:8132–9.
66. Albrecht SC, Barata AG, Großhans J, Teleman AA, Dick TP. In vivo mapping of hydrogen peroxide and oxidized glutathione reveals chemical and regional specificity of redox homeostasis. Cell Metab 2011;14:819–29.
67. Winterbourn CC. Toxicity of iron and hydrogen peroxide: the Fenton reaction. Toxicol Lett 1995;82–83:969–74.
68. Dixon SJ, Stockwell BR. The role of iron and reactive oxygen species in cell death. Nat Chem Biol 2014;10:9–17.
69. Dolma S, Lessnick SL, Hahn WC, Stockwell BR. Identification of genotype-selective antitumor agents using synthetic lethal chemical screening in engineered human tumor cells. Cancer Cell 2003;3:285–96.

70. Yang WS, Sriramaratnam R, Welsch ME, Shimada K, Skouta R, Viswanathan VS, et al. Regulation of ferroptotic cancer cell death by GPX4. Cell 2014;156: 317–31.
71. Yang WS, Kim KJ, Gaschler MM, Patel M, Shchepinov MS, Stockwell BR. Peroxidation of polyunsaturated fatty acids by lipoxygenases drives ferroptosis. Proc Natl Acad Sci 2016;113:E4966–E4975.
72. Yuan H, Li X, Zhang X, Kang R, Tang D. CISD1 inhibits ferroptosis by protection against mitochondrial lipid peroxidation. Biochem Biophys Res Commun 2016; 478:838–44.
73. Koppula P, Zhang Y, Zhuang L, Gan B. Amino acid transporter SLC7A11/xCT at the crossroads of regulating redox homeostasis and nutrient dependency of cancer. Cancer Commun (Lond) 2018;38:12.
74. Voorhees PM, Schlossman RL, Gasparetto CJ, Berdeja JG, Morris J, Jacobstein DA, et al. An open-label, dose escalation, multi-center phase 1 study of PRLX 93936, an agent synthetically active against the activated ras pathway, in the treatment of relapsed or relapsed and refractory multiple myeloma. Blood 2014; 124:2140.
75. Ramanathan RK, Rosen PJ, Wagner AJ, Sahasrabudhe S, Weiss GJ, Lee P, et al. A phase I pharmacodynamic and pharmacokinetic study of a Ras inhibitor, PRLX 93936, in patients with advanced solid tumors. J Clin Oncol 2010;28:e13042–.
76. Ohman KA, Hashim YM, Vangveravong S, Nywening TM, Cullinan DR, Goedegebuure SP, et al. Conjugation to the sigma-2 ligand SV119 overcomes uptake blockade and converts dm-Erastin into a potent pancreatic cancer therapeutic. Oncotarget 2016;7:33529–41.
77. Hashim YM, Spitzer D, Vangveravong S, Hornick MC, Garg G, Hornick JR, et al. Targeted pancreatic cancer therapy with the small molecule drug conjugate SW IV-134. Mol Oncol 2014;8:956–67.
78. Nielsen TO, Poulin NM, Ladanyi M. Synovial sarcoma: Recent discoveries as a roadmap to new avenues for therapy. Cancer Discov 2015;5:124–34.
79. Mayers JR, Torrence ME, Danai LV, Papagiannakopoulos T, Davidson SM, Bauer MR, et al. Tissue of origin dictates branched-chain amino acid metabolism in mutant Kras-driven cancers. Science (80-) 2016;353:1161–5.
80. Vander Heiden MG, DeBerardinis RJ. Understanding the intersections between metabolism and cancer biology. Cell 2017;168:657–69.
81. Intlekofer AM, Finley LWS. Metabolic signatures of cancer cells and stem cells. Nat Metab 2019;1:177–88.
82. Harris IS, Treloar AE, Inoue S, Sasaki M, Gorrini C, Lee KC, et al. Glutathione and thioredoxin antioxidant pathways synergize to drive cancer initiation and progression. Cancer Cell 2015;27:211–22.
83. Kumar C, Igbaria A, D'Autreaux B, Planson AG, Junot C, Godat E, et al. Glutathione revisited: a vital function in iron metabolism and ancillary role in thiol-redox control. EMBO J 2011;30:2044–56.
84. Floberg JM, Schwarz JK. Manipulation of glucose and hydroperoxide metabolism to improve radiation response. Semin Radiat Oncol 2019;29:33–41.
85. Li L, Fath MA, Scarbrough PM, Watson WH, Spitz DR. Combined inhibition of glycolysis, the pentose cycle, and thioredoxin metabolism selectively increases cytotoxicity and oxidative stress in human breast and prostate cancer. Redox Biol 2015;4:127–35.
86. Hrabe JE, O'Leary BR, Fath MA, Rodman SN, Button AM, Domann FE, et al. Disruption of thioredoxin metabolism enhances the toxicity of transforming growth factor β-activated kinase 1 (TAK1) inhibition in KRAS-mutated colon cancer cells. Redox Biol 2015;5:319–27.
87. Su Y, Tatzel K, Wang X, Belt B, Binder P, Kuroki L, et al. Mesothelin's minimal MUC16 binding moiety converts TR3 into a potent cancer therapeutic via hierarchical binding events at the plasma membrane. Oncotarget 2016;7:31534–49.
88. Garg G, Vangveravong S, Zeng C, Collins L, Hornick M, Hashim Y, et al. Conjugation to a SMAC mimetic potentiates sigma-2 ligand induced tumor cell death in ovarian cancer. Mol Cancer 2014;13:1–13.
89. Hornick JR, Vangveravong S, Spitzer D, Abate C, Berardi F, Goedegebuure P, et al. Lysosomal membrane permeabilization is an early event in sigma-2 receptor ligand mediated cell death in pancreatic cancer. J Exp Clin Cancer Res 2012;31:1–11.
90. Spitzer D, Simon PO, Kashiwagi H, Xu J, Zeng C, Vangveravong S, et al. Use of multifunctional sigma-2 receptor ligand conjugates to trigger cancer-selective cell death signaling. Cancer Res 2012;72:201–9.
91. Kashiwagi H, McDunn JE, Simon PO, Goedegebuure PS, Vangveravong S, Chang K, et al. Sigma-2 receptor ligands potentiate conventional chemotherapies and improve survival in models of pancreatic adenocarcinoma. J Transl Med 2009;7:1–8.
92. Kashiwagi H, McDunn JE, Simon PO, Goedegebuure PS, Xu J, Jones L, et al. Selective sigma-2 ligands preferentially bind to pancreatic adenocarcinomas: applications in diagnostic imaging and therapy. Mol Cancer 2007;6:1–12.